

# Rapid Determination of Low-Thrust Spacecraft Reachable Sets in Two-Body and Cislunar Problems

Sean R. Bowerfind<sup>\*</sup> and Ehsan Taheri<sup>†</sup>  
*Auburn University, Auburn, AL, 36830*

The reachable set of controlled dynamical systems consist of the set of all possible reachable states from an initial condition, over a certain period of time under various control and operation constraints and exogenous disturbances. For space applications, determination of reachable sets is invaluable for trajectory planning, collision avoidance, ensuring safe and optimal performance in complex, real-world scenarios. Leveraging the connection between minimum-time and reachable sets, we propose a method for rapid determination of reachable sets for finite- and low-thrust spacecraft using an indirect minimum-time multi-stage formulation and the primer vector theory. Reachable set analyses are presented for a minimum-time low-thrust Earth-Mars rendezvous problem and for several cislunar applications under circular restricted three-body dynamics. For the Earth-Mars problem and thruster parameters, results indicate that the minimum-time solution lies within the feasible set of position vectors, but on the boundary of the reachable set of velocity vectors. For the cislunar problems, L2 Halo orbit and Lunar Gateway 9:2 NRHO are considered. Our results indicate that the reachable set of low-thrust spacecraft coincides with invariant manifolds existing in the multi-body dynamical environments.

## I. Introduction

Optimal control and robotics applications frequently use reachable set theory as a metric to assess cost and safety. In astrodynamics, solutions to reachability problems are useful for determining the spacecraft states that will lead to an inevitable collision or encounter, regardless of future collision avoidance maneuvers [1]. In the near Earth-orbit domain, the ability to accurately and rapidly compute the reachable set has significant implications in space-domain awareness to predict future spacecraft collisions and to generate optimal collision avoidance maneuvers. This is a problem currently facing all civil, commercial, and defense space-users. In 2022, the United States Space Force unveiled a new program under SpaceWERX titled “Orbital Prime”, whose intentions are to stimulate the development of the Space Logistics/On-orbit servicing (OSAM/ISAM) industries. The primary focus of this initiative is to develop technologies to perform satellite re-location, de-orbiting, space debris removal, and remote and close inspection [2]. Each of these tasks requires complex capabilities to map the Earth orbit environment. Current technology can detect more than 27,000

<sup>\*</sup>Ph.D. Student, Department of Aerospace Engineering, Auburn University, 141 Engineering Dr Auburn, AL 36849, AIAA Student Member.

<sup>†</sup>Assistant Professor, Department of Aerospace Engineering, Auburn University, 141 Engineering Dr Auburn, AL 36849, AIAA Senior Member.

spacecraft and debris in orbit [3], however, a framework for modeling each of these objects and determining their reachable sets at future time horizons is crucial to accomplishing the OSAM/ISAM tasks. Knowledge of an object's reachable set can be used to perform evasive maneuvers (in the case of the International Space Station) or to perform orbital rendezvous and docking (to accomplish many of the OSAM/ISAM tasks) [4]. Beyond low-Earth orbits, the ability to compute reachable sets is advantageous to cislunar [5] and interplanetary mission design, as reachable sets provide mission designers with information regarding future planetary encounters from a given set of initial conditions [6]. Future NASA deep-space missions with numerous planetary flybys could benefit substantially from knowledge about the reachable set of their respective spacecraft. For example, NASA's Europa Clipper, slotted to launch in October 2024, will orbit Jupiter and perform a projected 50 flybys of Europa [7]. With knowledge of a reachable set from an initial point in Jupiter's orbit, Europa Clipper can investigate low-thrust maneuvers that could encounter more of Jupiter's moons in addition to Europa to provide a higher scientific return on investment for the mission.

A reachable set is defined as the set of states that can be reached from a given initial condition within a specified time span. Determining the reachable set is a problem that suffers from the "curse of dimensionality" since the Hamilton-Jacobi-Bellman (HJB) equation [8], a partial differential equation (PDE), is traditionally used to determine reachable sets. The exact reachable set boundary can be found at the zero-level sets of the viscosity solution of an HJB problem [9]. Across all classes of systems, linear, time-invariant (LTI) systems have been the most thoroughly analyzed. Results of LTI studies have shown that an analytical solution for the reachable set exists for cases of convex polyhedral state and control spaces [10]. However, once constraints that lead to a nonconvex control space are introduced (common in astrodynamics problems), analytical solutions do not exist and numerical methods (i.e., *direct* and *indirect*) must be used instead [11]. Indirect methods will attempt to solve the viscosity solution of the HJB, while direct methods attempt to solve a (non-Hamiltonian) two-point boundary-value problem (TPBVP) [12, 13]. In 1980, Vinter showed how to approximate the reachability problem as a convex optimization problem and did the first study to demonstrate how to approximate the reachable set using a series of smoothing functions [14]. Determination of the reachable set becomes an increasingly difficult problem as the dimensionality of the problem and the number of control signals increases [15]. It rapidly becomes computationally infeasible to compute every possible trajectory variation through simulation alone [16]. Modern research has expanded these approximation techniques to generate over- or under- approximations for continuous time-linear systems [17], general nonlinear dynamics [18], and more complex systems [19].

In the field of astrodynamics, reachability problems for both chemical and electric propulsion spacecraft are studied. Chemical propulsion reachability largely focuses on single impulse maneuvers and has been studied extensively for the cislunar environment [20–33]. Multiple electric propulsion or continuous thrust problems have been proposed for low-Earth, cislunar, and interplanetary mission planning applications [13, 15, 34–37]. Other methods attempt to calculate reachable sets by utilizing passive  $\Delta V$  maneuvers such as gravity assists and solar radiation pressure in small-body proximity operations. [4, 6, 38–40].

For the chemical propulsion case, an on-orbit range equation is derived for  $\Delta V$  with  $J_2$  perturbations [41]. These results are used in [32] to demonstrate closed-form impulsive control schemes by computing a minimum  $\Delta V$  then solving a geometric path-planning problem. For the electric propulsion case, [42] derives continuous indirect equations incorporating ellipsoid uncertainty with no mass loss. Several studies, [43] and [44] formulate optimal control problems and directly solve the HJB equation to generate reachable sets in the CR3BP over short time horizons. Specifically, [43] takes a Poincaré section approach and details analysis with invariant manifolds and [44] utilizes a power-series approximation of the HJB to determine periodic orbit transfer trajectories. A cross-disciplined reachability-based trajectory design (RTD), developed by Kousik, has been used to perform safe path planning for quadcopters, wheeled-vehicles, and robotic manipulators [45], [46]. RTD computes the forward reachable set (FRS) of a vehicle offline using zonotope reachability [47]. The FRS is used in real time to perform obstacle avoidance maneuvering by comparing the FRS with an environment map that dictates the safe set. RTD uses this method to perform path planning in real time before feeding the safe trajectory to a low-level tracking controller. RTD has been successfully demonstrated in both simulation and hardware demonstrations.

Determination of the reachable sets of low-thrust trajectories can be achieved by considering minimum-time solutions [48]. For a spacecraft equipped with low-thrust propulsion system, this means that the thruster will always be operating at maximum thrust and only the direction of the thrust vector is subject to variations across the reachable set. Reachable points are possible only by trajectories that use a thruster at maximum magnitude for the entire time horizon (i.e., a minimum-time trajectory). In fact, there is a duality between minimum-time and minimum-thrust solutions [48]. Trajectories that characterize feasible sets (i.e., interior to the reachable set) will produce a bang-bang control profile, correspond to minimum-fuel trajectories for a fixed time horizon and thrust parameters. The boundary of reachable set is defined by minimum-time solutions and we only focus on the boundary of *reachable* sets corresponding to minimum-time trajectories due to notable simplifications and speedup achieved combined with the primer vector theory.

Our main contributions are as follows: First, we propose a rapid indirect multi-stage formulation (IMF) for determining the reachable set of low-thrust spacecraft by leveraging the theoretical connection between minimum-time trajectories and reachable sets. This theoretical connection leads to noticeable algorithmic simplification and speedup compared to the minimum-fuel method proposed in [49, 50]. We formulate all problems from a forward-reachable perspective that provides insights on the aforementioned spacecraft collision problems and celestial encounters. More specifically, the discussion and presentation of the details of the IMF is given, which is an automated first-order approximation algorithm that is capable of sampling the reachable set. This algorithm requires no initial guess (automated) and utilizes only one first-order integration to forward propagate the nonlinear equations of motion for each sample. Secondly, we present the low-thrust reachability results for interplanetary trajectory optimization. In particular, minimum-time, rendezvous-type, Earth-to-Mars (Earth-Mars) maneuvers for a low-thrust spacecraft are presented. We show how the results can be used to rapidly determine position and velocity reachability subject to additional initial

boundary constraints for a low-thrust Earth-Mars rendezvous trajectory optimization problem. In this context, the distinction between position- and velocity-reachability are highlighted. Thirdly, we applied the low-thrust reachability to a number of problems in the CR3BP of the Earth-Moon system. We demonstrate the versatility of this approach by generating novel results on the reachable set for a low-thrust spacecraft in cislunar space. We illustrate the unique evolution of the reachable set for a L2 Halo orbit and 9:2 NRHO. The last contribution of the paper is to offer theoretical insights into the behavior of the reachable sets in the CR3BP. We show that the reachable sets are connected to invariant manifolds of periodic orbits. The results also demonstrate the computational features of the proposed method.

The remainder of the paper is organized as follows. First, the IMF optimal control problem is introduced in Section II.A, which precedes discussions on the two-body equations of motion in Section II.B, the CR3BP in Section II.C, a derivation of minimum-time optimal control relations in Section II.D, and details on the application of initial boundary conditions in Section II.E. Next, we outline the rapid reachable set determination algorithm in Section III. Finally, results are presented for the two-body dynamics in Section IV and for the CR3BP in Section V. We add remarks on invariant manifolds in Section V.D to explain some trends identified within the CR3BP. Section VI presents a conclusion. In the remainder of the paper, vectors are denoted in boldface letters.

## II. Indirect Multi-Stage Formulation of Optimal Control Problems

### A. Indirect Multi-Stage Formulation

An IMF of OCPs is adopted, which offers notable computational advantages since it allows for dynamics, constraints, and even cost functions to vary between different stages. This is an important feature for the introduction of initial boundary conditions, since incorporation of boundary conditions is achieved through a different cost function to account for any mass discrepancies due to an impulse maneuver. The other reason for using an IMF is the ability to derive analytical expressions for control, but also the fact that the entire reachable set determination is based on linearization.

The IMF divides a complete trajectory into a series of trajectory stages, but “connects” each stage through a sequence of equality constraints (see Fig. 1). Each stage receives inputs of the states and controls from the previous stage, but independently optimizes control over only its respective stage [51]. The entire trajectory can be discretized into  $N$  stages and the  $i^{\text{th}}$  stage (for  $i \in \{1, \dots, N\}$ ) can be modeled with its dynamical system consisting of states,  $\mathbf{x} \in \mathbb{R}^{n_x}$ , controls,  $\mathbf{u} \in \mathbb{R}^{n_u}$ , and parameters,  $\mathbf{p} \in \mathbb{R}^{n_p}$ , where superscript is used to denote the stage index as,

$$\mathbf{x}^{i+1} = \mathbf{F}^i(\mathbf{x}^i, t^i, \mathbf{u}^i; \mathbf{p}), \quad \text{with} \quad \mathbf{F}^i = \mathbf{x}^i + \int_{t_i}^{t_{i+1}} \dot{\mathbf{x}} dt = \mathbf{x}^i + \int_{t_i}^{t_{i+1}} \mathbf{f}^{i-1}(\mathbf{x}, t, \mathbf{u}; \mathbf{p}) dt. \quad (1)$$

The IMF solves OCPs recursively, that is, stage  $i = 1$  is solved first, then  $i = 2, \dots, i = N$  until the solution to all stages are computed. The derivation of the optimal control expressions is similar to continuous-time indirect

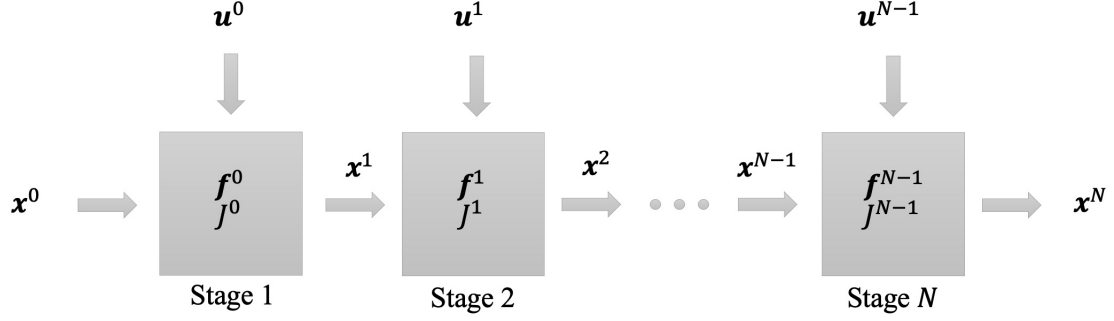


Fig. 1 Flowchart for a multi-stage formulation.

formulations, except for some additional notation bookkeeping to track stages. The cost function for an IMF is:

$$J = \phi(x^N, N) + \sum_i L^i(t^i, x^i, u^i), \quad (2)$$

where  $\phi$  denotes a final cost and  $L(\cdot)$  is the stage cost evaluated over the time span of each independent stage. The Hamiltonian of the complete trajectory can be written as the summation over the Hamiltonian of individual stages as,

$$H = \sum_i H^i, \quad \text{with} \quad H^i = (\lambda^{i+1})^\top F^i + L^i + \sum_k v_k C_k. \quad (3)$$

The costates,  $\lambda \in \mathbb{R}^{n_x}$ , are specified with an  $i + 1$  index for convenience in the implementation of the algorithm, which includes a backward-in-time integration for the costates. In Eq. (3),  $C_k$  and  $v_k$  indicate the  $k^{\text{th}}$  path constraint and its associated Lagrange multiplier (dimension of constraints,  $k$  depends on the problem and the constraints). For each stage, partial derivatives of the Hamiltonian with respect to states and controls can be formed as,

$$\frac{\partial H^i}{\partial x} = H_x^i = \lambda^i = (F_x^i)^\top \lambda^{i+1} + L_x^i + \sum_k v_k C_{k,x}, \quad \frac{\partial H^i}{\partial u} = H_u^i = \mathbf{0} = (F_u^i)^\top \lambda^{i+1} + L_u^i + \sum_k v_k C_{k,u}. \quad (4)$$

## B. Two-Body Equations of Motion

For the first results presented in this paper, the heliocentric phase of an Earth-Mars rendezvous problem (with zero hyperbolic excess velocity) will be considered and third-body perturbations are ignored. Let  $\mathbf{r} \in \mathbb{R}^3$  and  $\mathbf{v} \in \mathbb{R}^3$  denote the position and velocity vectors, respectively. Let  $\mathbf{x} = [\mathbf{r}^\top, \mathbf{v}^\top]^\top$  denote the state vector and let  $\hat{\boldsymbol{\alpha}}$  denote the thrust steering unit vector. the state dynamics can be written as [52].

$$\dot{\mathbf{x}} = \begin{bmatrix} \dot{\mathbf{r}} \\ \dot{\mathbf{v}} \end{bmatrix} = \begin{bmatrix} \mathbf{v} \\ -\frac{\mu}{\|\mathbf{r}\|^3} \mathbf{r} + \frac{T_{\max}}{m} \hat{\boldsymbol{\alpha}} \delta \end{bmatrix}, \quad (5)$$

where  $\mu$  denotes the gravitational parameter of the Sun,  $c = I_{\text{sp}}g_0$  is the net exhaust velocity, with  $I_{\text{sp}}$  denoting the specific impulse, and  $g_0$  being the gravitational acceleration at the Earth's surface.  $T_{\text{max}}$  is the maximum thrust of the propulsion system operating in a thrust direction,  $\hat{\mathbf{a}} \in \mathbb{R}^3$ , with a throttle setting of  $\delta \in [0, 1]$ . In a minimum-fuel solution, the optimal control of a low-thrust propulsion system will involve finding both  $\hat{\mathbf{a}}$  and  $\delta$ , however, for a minimum-time solution, it is known that the engine has to operate at maximum throttle during the entire trajectory ( $\delta(t) = 1 \forall t \in [t_0, t_f]$ ) [53]. Thus, different minimum-time trajectories can be generated by varying thrust directions,  $\hat{\mathbf{a}}$  all of which characterize the low-thrust reachable set. The spacecraft mass,  $m$ , can be calculated as,  $m(t) = m_0 - \frac{T_{\text{max}}}{c}(t - t_0)$ . This minimum-time formulation allows the control vector,  $\mathbf{u} \in \mathbb{R}^3$ , to be stated simply as

$$\mathbf{u}(t) = \hat{\mathbf{a}}(t), \quad \|\hat{\mathbf{a}}(t)\| = 1. \quad (6)$$

Alternative approaches for modeling a low-thrust spacecraft invoke a minimum-fuel formulation, which necessitates the tracking of mass and additional parameterization of the control vector by including both thrust magnitude and thrust direction [54]. A similar reachable set determination method proposed by Patel in Refs. [49, 50, 55, 56] formulates a minimum-fuel problem and utilizes an inverse mass parameter,  $n = 1/m$ , to track mass flow. This method resolves some common problems encountered when using standard mass flow dynamics,  $\dot{m} = -\|\mathbf{T}\|/c$ , in that this relation is non-differentiable when  $\mathbf{T} = \mathbf{0}$ .

### C. Circular Restricted Three Body Problem

The reachable set analysis of spacecraft in three-body dynamics has significant utility for near-term cislunar reachability applications. We consider the CR3BP model, which as will be shown offers more insights into the class of solutions that are obtained. That is, the problem utilizes the rotating synodic frame where the motion of the two primaries is assumed to be circular and the mass of the third object is negligible. The CR3BP is normalized such that the distance between the two primaries, total mass of the system, and mean motion of the two primary masses is unity. The characteristic length is defined as the distance between the two primaries,  $l^*$ , characteristic mass is defined as the sum of the masses of the two primaries,  $m^* = m_1 + m_2$ , and characteristic time is the mean motion of the primary system,  $t^* = \sqrt{\frac{l^{*3}}{Gm^*}}$ , where  $G$  is the universal gravitational constant. In the CR3BP, the mass ratio is an important parameter used to differentiate between different systems, defined as,  $\mu = \frac{m_2}{m^*}$ . These characteristic values for the Earth-Moon system are as follows [57]:  $l^* = 3.844 \times 10^5$  km,  $m^* = 6.0458 \times 10^{24}$  kg,  $t^* = 375200$  seconds, and  $\mu = 0.0121505856$ .

In addition to the natural dynamics involving the motion of the two primaries, additional terms involving spacecraft mass and thrust must be normalized. Since the mass of the spacecraft was assumed negligible for the CR3BP derivation, these terms must be normalized by the initial mass of the spacecraft to avoid numerical issues. Since  $m$  does not explicitly depend on the state,  $\mathbf{x}$ , we normalize control accordingly,  $m_{s/c}^* = m_{0,s/c}$  and  $T_{s/c}^* = \frac{m_{s/c}^* I^*}{t^{*2}}$ . Incorporating the

geometry of the CR3BP presented in [58], the origin of the rotating frame is the barycenter of the two primaries and the  $x$ -axis is the vector collinear with the center of mass of the two primaries. Also,  $m_1$  and  $m_2$ , are located at distances  $-\mu$  and  $1 - \mu$  along the  $x$ -axis, respectively. Let  $\hat{\boldsymbol{\alpha}} = [\alpha_x, \alpha_y, \alpha_z]^\top$  denote the thrust steering unit vector. The equations of motion for a low-thrust spacecraft in normalized coordinates are

$$\dot{\mathbf{x}} = \begin{bmatrix} \dot{\mathbf{r}} \\ \dot{\mathbf{v}} \end{bmatrix} = \begin{bmatrix} \mathbf{v} \\ x + 2v_y - \frac{(1-\mu)(x+\mu)}{r_1^3} + \frac{\mu(x+\mu-1)}{r_2^3} + \frac{T_{\max}}{m}\alpha_x \\ y - 2v_x - \frac{(1-\mu)y}{r_1^3} - \frac{\mu y}{r_2^3} + \frac{T_{\max}}{m}\alpha_y \\ -\frac{(1-\mu)z}{r_1^3} - \frac{\mu z}{r_2^3} + \frac{T_{\max}}{m}\alpha_z \end{bmatrix}, \quad (7)$$

where  $r_1 = \sqrt{(x+\mu)^2 + y^2 + z^2}$  and  $r_2 = \sqrt{(x+\mu-1)^2 + y^2 + z^2}$  denote the distances from the Earth and Moon, respectively. The state and control vectors and the control constraint ( $\|\hat{\boldsymbol{\alpha}}\| = 1$ ) are consistent for both the two-body and CR3BP dynamics.

#### D. Formulation of Minimum-Time Optimal Control Problems

Let  $\Delta t$  denote the stage time interval, where  $\Delta t$  is held constant across all stages. The objective function is,

$$\text{minimize } J = \sum_i \Delta t. \quad (8)$$

The Hamiltonian for each stage from the single-stage dynamics,  $\mathbf{F}^i$ , objective function,  $J$ , and the constraint from Eq. (6) can be written as,

$$H^i = \Delta t + (\mathbf{F}^i)^\top \boldsymbol{\lambda}^{i+1} + \nu_1 (\|\hat{\boldsymbol{\alpha}}^i\| - 1), \quad (9)$$

where  $\nu_1$  is a Lagrange multiplier used for augmenting thrust constraints to the Hamiltonian. The value of  $\nu_1$  must be determined as part of the solution procedure. Let  $\boldsymbol{\lambda}^\top = [\boldsymbol{\lambda}_x^\top, \boldsymbol{\lambda}_v^\top]$  denote the costate vector. The costate differential equations are derived by forming the partial derivative of the Hamiltonian in Eq. (9) with respect to the state vector,  $\mathbf{x}$ , written as (we use  $\mathbf{F}_x^{i,\top} = (\mathbf{F}_x^i)^\top$ ),

$$\frac{\partial H^i}{\partial \mathbf{x}} = H_x^i = \boldsymbol{\lambda}^i = \mathbf{F}_x^{i,\top} \boldsymbol{\lambda}^{i+1}. \quad (10)$$

Note that Eq. (10) is indeed set up to be integrated backward with respect to time, since the costate vector from the previous stage,  $\boldsymbol{\lambda}^{i+1}$ , is on the right-hand side. This backward-in-time step is related to the negative sign in  $\dot{\boldsymbol{\lambda}} = -[\partial H / \partial \mathbf{x}]^\top$  for continuous-time relations obtained from applying the Euler-Lagrange equation in a standard

indirect method. The control law is found from the partial derivative of Eq. (9) with respect to the control vector,  $\mathbf{u}$ , as,

$$\frac{\partial H^i}{\partial \mathbf{u}} = H_{\mathbf{u}}^i = \mathbf{0} = \mathbf{F}_{\mathbf{u}}^{\top} \boldsymbol{\lambda}^{i+1} + \nu_1 \left( \frac{\hat{\boldsymbol{\alpha}}^i}{\|\hat{\boldsymbol{\alpha}}^i\|} \right). \quad (11)$$

In Eqs. (10) and (11), matrices  $\mathbf{F}_{\mathbf{x}}$  and  $\mathbf{F}_{\mathbf{u}}$  denote the state transition and sensitivity matrices, respectively, for linear systems [59]. To evaluate  $\mathbf{F}_{\mathbf{x}}$  and  $\mathbf{F}_{\mathbf{u}}$  matrices, their matrix differential equations must be propagated through each stage to evaluate their values at the final time of each stage. Let  $\Phi = \mathbf{F}_{\mathbf{x}}$  and  $\Omega = \mathbf{F}_{\mathbf{u}}$ , the matrix differential equations [59] can be written as,

$$\dot{\Phi}(t, t_i) = \mathbb{A}(t)\Phi(t, t_i), \quad \dot{\Omega}(t, t_i) = \mathbb{A}(t)\Omega(t, t_i) + \mathbb{C}(t), \quad (12)$$

where the matrices  $\mathbb{A}(t) \in \mathbb{R}^{n_x \times n_x}$  and  $\mathbb{C}(t) \in \mathbb{R}^{n_x \times n_u}$  can be derived as,

$$\mathbb{A}(t) = \frac{\partial \dot{\mathbf{x}}}{\partial \mathbf{x}} = \begin{bmatrix} \mathbf{0} & \mathbf{I} \\ \frac{\partial \dot{\mathbf{v}}}{\partial \mathbf{r}} & \mathbf{0} \end{bmatrix}, \quad \mathbb{C}(t) = \frac{\partial \dot{\mathbf{x}}}{\partial \mathbf{u}} = \begin{bmatrix} \mathbf{0} \\ \text{diag}(\frac{T_{\max}}{m}) \end{bmatrix}. \quad (13)$$

The IMF notation can be updated and we can rewrite Eq. (12) in an integral form as,

$$\mathbf{F}_{\mathbf{x}}^i = \frac{\partial \mathbf{x}^{i+1}}{\partial \mathbf{x}^i} = \Phi(t^{i+1}, t^i) = \int_{t^i}^{t^{i+1}} \mathbb{A}(t)\Phi(t, t^i) dt, \quad \mathbf{F}_{\mathbf{u}}^i = \frac{\partial \mathbf{x}^{i+1}}{\partial \mathbf{u}^i} = \Omega(t^{i+1}, t^i) = \int_{t^i}^{t^{i+1}} [\mathbb{A}(t)\Omega(t, t^i) + \mathbb{C}(t)] dt, \quad (14)$$

with the initial conditions defined as  $\Phi(t^i, t^i) = \mathbf{I}$  and  $\Omega(t^i, t^i) = \mathbf{0}$  (with  $\mathbf{I}$  denoting the  $n_x \times n_x$  identity matrix). The final step of the IMF is to solve Eq. (11) for an optimal control law. Applying the strong form of optimality, such that Eq. (11) is equal to zero, leads to

$$\mathbf{0} = \mathbf{F}_{\mathbf{u}}^{\top} \boldsymbol{\lambda}^{i+1} + \nu_1 \frac{\hat{\boldsymbol{\alpha}}^i}{\|\hat{\boldsymbol{\alpha}}^i\|}, \rightarrow -\frac{\mathbf{F}_{\mathbf{u}}^{\top} \boldsymbol{\lambda}^{i+1}}{\nu_1} = \frac{\hat{\boldsymbol{\alpha}}^i}{\|\hat{\boldsymbol{\alpha}}^i\|} = \hat{\boldsymbol{\alpha}}^i. \quad (15)$$

Using the definition of  $\hat{\boldsymbol{\alpha}}$ ,  $\nu_1$  must be equal to  $\|\mathbf{F}_{\mathbf{u}}^{\top} \boldsymbol{\lambda}^{i+1}\|$ , which yields the familiar primer vector optimal control law,

$$\hat{\boldsymbol{\alpha}}^i = -\frac{\mathbf{F}_{\mathbf{u}}^{i, \top} \boldsymbol{\lambda}^{i+1}}{\|\mathbf{F}_{\mathbf{u}}^{i, \top} \boldsymbol{\lambda}^{i+1}\|}. \quad (16)$$

## E. Initial Boundary Conditions

The IMF allows for imposing constraints on only one stage, or even using a different cost functional across different stages. We take advantage of this feature to present the framework for imposing position and velocity ellipsoid uncertainty constraints (per the method of [42]) as well as an impulse maneuver at the simulation start time, adapting the

work presented in [50, 56]. However, we present related numerical results to the Earth-Mars problem. To accomplish this, we add a pseudo-zero stage that converts the reference trajectory initial states,  $\mathbf{r}^{\text{ref}}$  and  $\mathbf{v}^{\text{ref}}$ , into perturbed initial states,  $\mathbf{r}^*$  and  $\mathbf{v}^*$ . We use a matrix-mapping technique to account for the variation in each of the states as,

$$\begin{bmatrix} \mathbf{r}^* \\ \mathbf{v}^* \end{bmatrix} = \begin{bmatrix} \mathbf{r}^{\text{ref}} \\ \mathbf{v}^{\text{ref}} \end{bmatrix} + \begin{bmatrix} \mathbf{I} & \mathbf{0} & \mathbf{0} \\ \mathbf{0} & \mathbf{I} & \mathbf{I} \end{bmatrix} \begin{bmatrix} \delta \mathbf{r} \\ \delta \mathbf{v}_1 \\ \delta \mathbf{v}_2 \end{bmatrix}. \quad (17)$$

Our goal is to solve for  $[\delta \mathbf{r}, \delta \mathbf{v}_1, \delta \mathbf{v}_2]^\top$ , which are the states associated with variations from the reference state. In Eq. (17),  $\delta \mathbf{r}$  and  $\delta \mathbf{v}_1$  are associated with ellipsoid position and velocity uncertainty constraints. In addition,  $\Delta V$  impulse maneuver constraints are handled through  $\delta \mathbf{v}_2$ . An additional cost function is required to account for the variation in initial mass due to the impulse maneuver. We select Tsolkovsky rocket equation as the cost function to track the mass consumed due to this impulsive maneuver as,  $L^* = m_0 - m_0 e^{-\frac{\Delta V}{c}}$ . The (pseudo-zero stage) Hamiltonian is formed as,

$$H^* = m_0 - m_0 e^{-\frac{\Delta V}{c}} + \boldsymbol{\lambda}^\top [\mathbf{r}^{*\top}, \mathbf{v}^{*\top}]^\top + \sum_k v_k C_k. \quad (18)$$

Next, we must express  $C_k$  for both types of constraints. We use ellipsoid uncertainty constraint formulations from [42] to express the position and velocity uncertainty in the form of equality constraints as,

$$\frac{1}{2} \delta \mathbf{r}^\top \mathbb{E}_r \delta \mathbf{r} - \frac{1}{2} r_{\text{ref}}^2 = 0, \quad \frac{1}{2} \delta \mathbf{v}_1^\top \mathbb{E}_v \delta \mathbf{v}_1 - \frac{1}{2} v_{\text{ref}}^2 = 0, \quad (19)$$

where  $\mathbb{E}_r$  and  $\mathbb{E}_v$  are matrices determining the major axes of the uncertainty ellipsoid. We need expressions for  $\delta \mathbf{r}$  and  $\delta \mathbf{v}_1$  to successfully implement constraints in Eq. (19). Computing the partial derivative of  $H^*$  with respect to  $\delta \mathbf{r}$  gives

$$\frac{\partial H^*}{\partial \delta \mathbf{r}} = H_{\delta \mathbf{r}}^* = \mathbf{0} = \boldsymbol{\lambda}_r + v_1 \mathbb{E}_r \delta \mathbf{r}, \rightarrow \delta \mathbf{r} = - (v_1 \mathbb{E}_r)^{-1} \boldsymbol{\lambda}_r, \quad (20)$$

where  $\boldsymbol{\lambda}_r$  is the pseudo-zero stage costates associated with the position vector. Substituting Eq. (20) into the position ellipsoid constraint, Eq. (19), yields an expression for  $v_1$ , which can be written as,

$$0 = \frac{1}{2} r_{\text{ref}}^2 - \frac{1}{2} \frac{\boldsymbol{\lambda}_r^\top \mathbb{E}_r^{-1} \boldsymbol{\lambda}_r}{v_1^2}, \rightarrow v_1 = \frac{\boldsymbol{\lambda}_r^\top \mathbb{E}_r^{-1} \boldsymbol{\lambda}_r}{r_{\text{ref}}^2}. \quad (21)$$

Substituting  $v_1$  into Eq. (20) gives the final equation as,

$$\delta \mathbf{r} = -r_{\text{ref}} \frac{\mathbb{E}_r^{-1} \boldsymbol{\lambda}_r}{\sqrt{\boldsymbol{\lambda}_r^\top \mathbb{E}_r^{-1} \boldsymbol{\lambda}_r}}. \quad (22)$$

All parameters in Eq. (22) are given, aided by the backwards integration in the second stage of the algorithm, which yields the costates,  $\boldsymbol{\lambda}_r$ . The initial condition position uncertainty constraint can be implemented. It is possible to follow the same process to obtain a solution for  $\delta \mathbf{v}_1$  as,

$$H_{\delta \mathbf{v}_1}^* = \mathbf{0} = \boldsymbol{\lambda}_v + v_2 \mathbb{E}_v \delta \mathbf{v}_1, \quad \delta \mathbf{v}_1 = -v_{\text{ref}} \frac{\mathbb{E}_v^{-1} \boldsymbol{\lambda}_v}{\sqrt{\boldsymbol{\lambda}_v^\top \mathbb{E}_v^{-1} \boldsymbol{\lambda}_v}}. \quad (23)$$

Equations (22) and (23) are analytical closed-form expressions for the change in initial conditions due to an ellipsoid uncertainty. These changes can be implemented in the reachable set algorithm without any structural modification to the algorithm (see Eq. (17)). The other type of scenario is the  $\Delta V$  impulse maneuver, which involves a separate boundary condition, since one must allow the magnitude of the  $\Delta V$  impulse to take values less than or equal to the maximum capability of the propulsion system,  $\Delta V_{\text{max}}$ . This constraint associated with the initial impulse can be written as,

$$\frac{1}{2} \delta \mathbf{v}_2^\top \delta \mathbf{v}_2 - \frac{1}{2} \Delta V_{\text{max}}^2 \leq 0. \quad (24)$$

The derivation of the closed-form solutions for these constraints is more involved due to the introduction of an inequality constraint that can be active or inactive. A complete derivation of the solution for  $\delta \mathbf{v}_2$  and  $\Delta V$  is given in the Appendix. However, if the inequality constraint is active, then we have the following two relations

$$\Delta V = \Delta V_{\text{max}}, \quad \delta \mathbf{v}_2 = -\Delta V_{\text{max}} \frac{\boldsymbol{\lambda}_v}{\|\boldsymbol{\lambda}_v\|}. \quad (25)$$

If the inequality constraint is not active, the optimal solution can be derived as,

$$\Delta V = -c \ln \left( \frac{\|\boldsymbol{\lambda}_v\| c + \sqrt{\|\boldsymbol{\lambda}_v\|^2 c^2}}{2m_0} \right), \quad \delta \mathbf{v}_2 = c \ln \left( \frac{\|\boldsymbol{\lambda}_v\| c + \sqrt{\|\boldsymbol{\lambda}_v\|^2 c^2}}{2m_0} \right) \frac{\boldsymbol{\lambda}_v}{\|\boldsymbol{\lambda}_v\|}. \quad (26)$$

The final step is to address the initial mass perturbation due to an impulse maneuver, which can be written as,  $\delta m = m_0 - m_0 e^{-\frac{\Delta V}{c}}$  with  $\Delta V$  becoming the computed value using the logic presented above. Finally, we need to update the initial mass as,  $m^* = m_0 + \delta m$ . We emphasize that the analytical solutions for an initial condition variation due to an impulse maneuver are only functions of the costates and other constants specified by the problem. This makes implementation of these types of constraints simple given the algorithm structure (i.e, treating stages differently).

### III. Reachable Set Determination Algorithm

This section presents details and schematics for the implementation of the reachable set algorithm, which consists of three main phases. First, a zero-thrust reference trajectory is used to obtain all reference states, state transition matrices, and sensitivity matrices corresponding to the reference trajectory. Second, a sufficiently large number of costates (at the final stage,  $N$ ) are sampled from a 6-dimensional unit ball corresponding to the costates associated with the position and velocity vectors. For each sampled costate vector, the costates are integrated backward in time, using the costate update mapping in Eq. (10), until the initial stage. Using the costates, control laws given by Eq. (16) are computed and stored. Last, the reachable set is reconstructed using a forward-in-time integration of the fully *nonlinear* state dynamics with the computed optimal control. The sampling-based aspect of the algorithm allows for thousands of reachable trajectories to be generated rapidly and in a parallel manner. Note that for each trajectory there is only one numerical integration and no optimization solver is used (as opposed to a direct optimal control method).

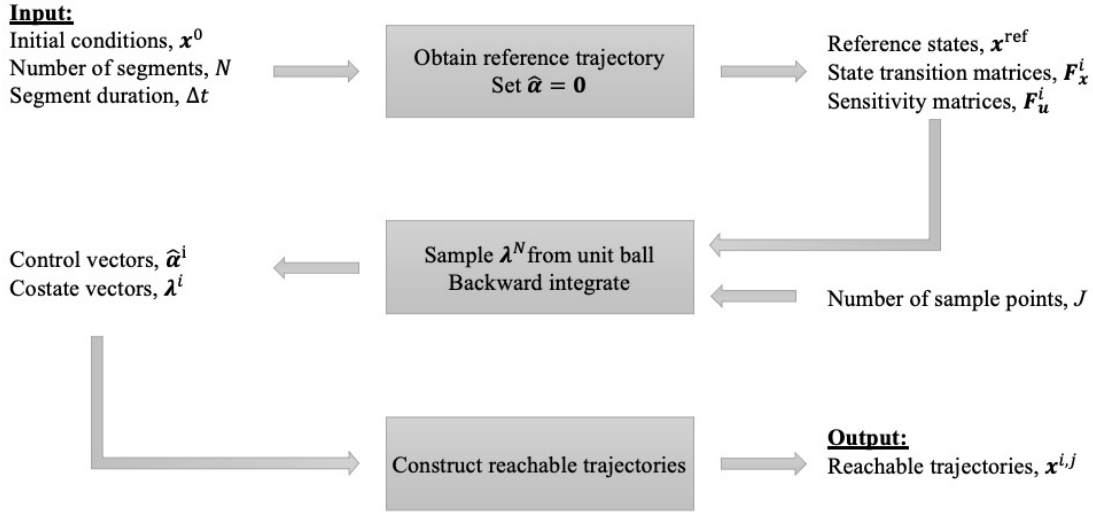


Fig. 2 Flowchart for the reachable set determination algorithm.

When selecting a reference trajectory, we select a zero-thrust (i.e., ballistic) trajectory. This is due to a trivial solution of the OCP in which  $\lambda^N = \mathbf{0}$ , causing  $\{\mathbf{u}_i\}_i^N = \mathbf{0}$ . Integrate the system dynamics forward-in-time from initial conditions  $\mathbf{x}^0$  with no control to obtain the reference trajectory,  $\mathbf{x}^{\text{ref}}$ , and  $\{\mathbf{F}_x^i\}_i^N$  and  $\{\mathbf{F}_u^i\}_i^N$  matrices.

Next, we sample terminal stage costates  $\lambda^N$  from a 6-dimensional unit ball (i.e.,  $\|\lambda^N\| = 1$ ). The reason we uniformly sample  $\lambda^N$  is due to the control law in Eq. (16), which indicates that the magnitude of  $\lambda^N$  does not matter (the control law is homogenous in costates); hence, a reasonable method to determine these values is to uniformly sample them from a unit ball. All previous stage costates are recovered, backwards in time, from a recursive matrix multiplication outlined in Eq. 10. The optimal control can be computed from Eq. (16) and a final forward-in-time integration is used to produce

the entire reachable set. The indices  $i$  and  $j$  in Fig. 2 indicate the  $i^{\text{th}}$ -stage variable quantity and the  $j^{\text{th}}$  trajectory forming the reachable set. The proposed minimum-time reachable set determination algorithm is outlined in Algorithm 1.

---

**Algorithm 1:** Reachable Set Determination

---

```

Result:  $x^{i,j}$  Reachable Trajectories
 $x^0 \leftarrow$  Initial Conditions;
 $p \leftarrow$  Constant Parameters;
 $N \leftarrow$  Number of Segments;
 $\Delta t \leftarrow$  Segment Duration;
 $J \leftarrow$  Number of sampled reachable points;
 $u^{\text{ref}} \leftarrow \mathbf{0}$ ;
 $t^i \leftarrow 0$ ;
while  $i = 0; i < N; i \leftarrow i + 1$  do
     $x^{i+1}, F_x^i, F_u^i \leftarrow F^i(x^i, u^{\text{ref}}, t^i, t^i + \Delta t, p)$ ;           /* Unpowered reference trajectory */
     $x^i \leftarrow x^{i+1}$ ;
     $t^i \leftarrow t^i + \Delta t$ ;
end
for  $j = 1 : J$  do
     $\lambda^N \leftarrow$  Sampled from Unit Ball;
     $i \leftarrow N$ ;
    while  $i = N; i \geq 1; i \leftarrow i - 1$  do
         $\hat{\alpha}^i \leftarrow -\frac{F_u^{i,T} \lambda^{i+1}}{\|F_u^{i,T} \lambda^{i+1}\|}$ ;           /* Optimal unit thrust steering vector */
         $\lambda^i \leftarrow F_x^{i,T} \lambda^{i+1}$ ;
    end
end
for  $j = 1 : J$  do
    while  $i = 0; i < N; i \leftarrow i + 1$  do
        if  $i = 0$  then
             $\delta r \leftarrow$  Eq. (20);
             $\delta v_1 \leftarrow$  Eq. (23);
             $\Delta V \leftarrow \Delta V_{\text{max}}$ ;
            if Eq. (32)  $> 0$  then
                 $\delta v_2, \Delta V \leftarrow$  Eq. (25);
            else
                 $\delta v_2, \Delta V \leftarrow$  Eq. (26);
            end
             $x^i \leftarrow$  Eq. (17);
        end
         $x^{i+1,j} \leftarrow F^i(x^i, \hat{\alpha}^{i,j}, t^i, t^i + \Delta t, p)$ ;           /* Reconstruct reachable trajectories */
         $x^i \leftarrow x^{i+1,j}$ ;
         $t^i \leftarrow t^i + \Delta t$ ;
    end
     $j \leftarrow j + 1$ ;
end

```

---

The proposed algorithm shares multiple aspects with a recent minimum-time based algorithm by Patel in [56], but we briefly discuss some key differences between the method dubbed ‘‘FFOE’’ and our proposed algorithm. First, FFOE utilizes a cost function designed to maximize final state in a unit-ball sampled direction, whereas, our proposed method

formulates a minimum-time IMF problem that allows direct comparison with the solution to a minimum-time OCP (see Sec. IV.B). Additionally, our formulation simplifies the dynamics by removing mass and its costate differential equations from the set of state-costate vector. This is aided by the minimum-time formation, since it is known that mass can be integrated analytically using thrust and time of flight [53]. Ref. [56] tracks inverse mass, which increases the dimensionality of the FFOE and leads to a longer computational time compared to the proposed algorithm (independent of the platform and programming language). Last, [56] formulates an impulse maneuver initial constraint by assuming that the applied  $\Delta V$  is equivalent to  $\Delta V_{\max}$  of the spacecraft. Our proposed method allows  $\Delta V$  taking any value less than or equal to  $\Delta V_{\max}$  at the expense of additional logic in the algorithm (see Appendix VII)

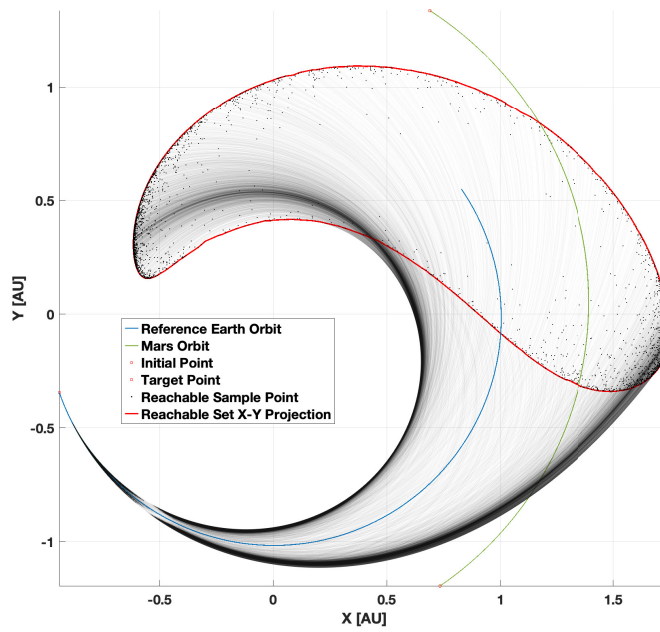
Nevertheless, we can use the combined observations from this study and [56] to draw conclusions on the shortcomings of a “sampling-type” reachable set estimation method. In general, the algorithm accuracy begins to deteriorate over long time horizons *unless* the number of sample points increases. Additionally, since the core of this method is a linearization about an unpowered reference trajectory, we expect that as the ratio of the acceleration produced by the propulsion to the natural acceleration due to gravity of the gravitational body(s) increases, the accuracy of the reachable set algorithm will decrease. These issues were also identified in [56] in which FFOE was used in an iterative manner where each sample trajectory was linearized about and the reachable set recomputed, however this method exhibited diminishing returns and numerical stability issues.

## IV. Two-Body Dynamics Results

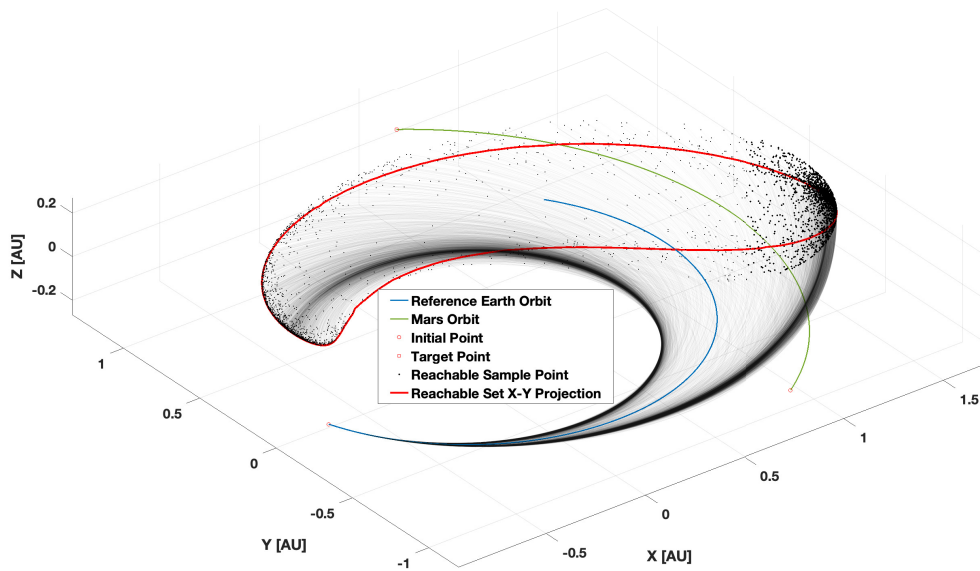
The results that have been obtained for the rapid reachability and rendezvous determination problem for a minimum-time Earth-Mars transfer are presented in this section. This example is taken from [60]. For all results,  $T_{\max} = 0.5$  Newton,  $I_{\text{sp}} = 3000$  seconds, and  $m_0 = 1000$  kg. The initial position and velocity vectors are  $\mathbf{r} = [-140699693; -51614428; 980]^T$  km and  $\mathbf{v} = [9.774596; -28.07828; 4.337725\text{E-}4]^T$  km/s, respectively, corresponding to a departure Epoch of April 10<sup>th</sup>, 2007. Segment duration,  $\Delta t$  is set to 86400 seconds. The reachable set algorithm was implemented in MATLAB on a 2018 MacBook Pro with a quad-core 2.3 GHz processor using parallel computing capabilities with 4 CPU cores. Additionally, MATLAB’s integrated code compiler was used to generate MEX files to speed up the algorithm. NASA’s spice toolkit was used for accessing DE440 planetary ephemerides. Computations are completed in the J2000 ecliptic reference frame centered at the solar system barycenter.

### A. Reachable set analysis for a fixed time horizon

We consider a time horizon of 200 days with a total of 5000 sample trajectories. This simulation completed in 13.61 seconds, which demonstrates rapid trajectory generation ability with 2.72 milliseconds per trajectory. The first, and most important, observation from Fig. 3a is that for the time span of 200 days, a portion of the Mars orbit is within the reachable set. However, the position of Mars (red square) is not within the reachable set (red). A longer time of flight is



(a) 2D view



(b) 3D view

**Fig. 3** Position reachable set over a 200-day time horizon with 5000 sample trajectories.

required for Mars to become reachable. The reference trajectory (blue line) is equivalent to the orbit of the Earth, since no control is applied. In Fig. 3a, AU stands for the astronomical unit ( $AU = 149 \times 10^6$  km).

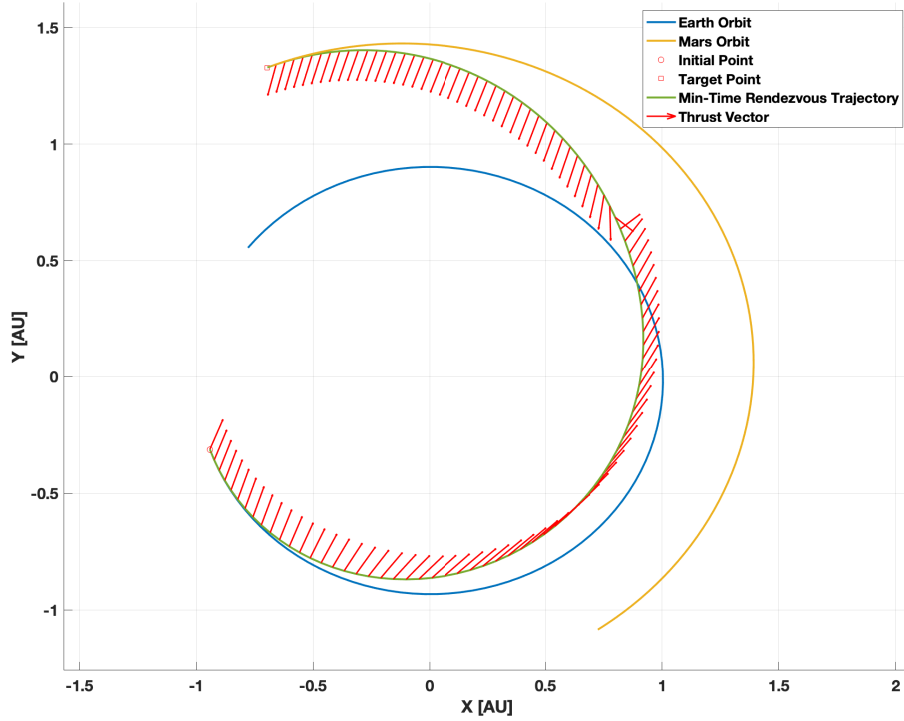
Figure 3b depicts a three-dimensional (3D) view of the reachable set, which is a deformed ellipsoid-like 3D shape created by the endpoint of all reachable trajectories. A funnel-like structure exists as we plot the time history of all reachable trajectories (light gray lines), we refer to this as the reachable funnel. The boundary points of the reachable funnel act as a time history of all reachable sets within a 200-day time span. The feasible set and feasible funnel are all the position states classified as the interior of the reachable set and reachable funnel. As the time of flight increases, the number of sample trajectories has to be increased because for long-time-horizon maneuvers the volume of the reachable set expands rapidly, so more sample points are required to construct an accurate approximation of the reachable set.

### **B. Reachable set comparison with the solution from a direct formulation**

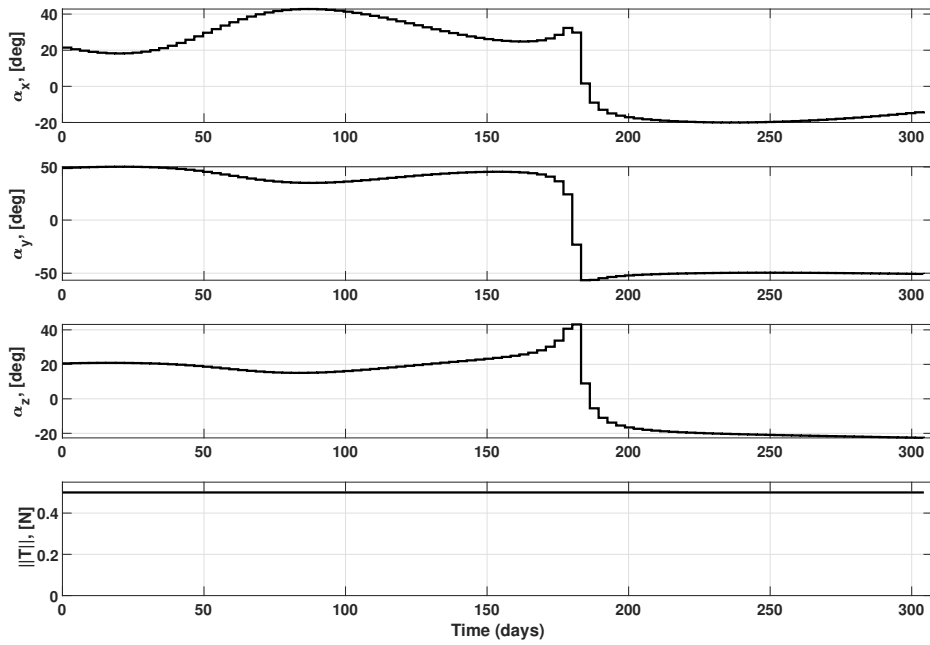
We seek to validate the accuracy of the reachable set estimate by comparing the results in Sec. IV.A with a minimum-time trajectory optimization problem. We solve a minimum-time direct OCP using the same initial conditions listed above. The minimum-time Earth-Mars OCP was solved using CasADi [61]), the resulting optimal trajectory and control are presented in Figure 4. Observe that the propulsion system is operating at maximum thrust for the duration of the flight, and only the thrust direction (red arrows) in Figure 4a varies. The minimum-time Earth-Mars problem, when solved, resulted in a trajectory with a time of flight of 307 days. The trajectory is also leveraging Oberth effect (i.e., it falls into the gravitational well of the Sun to maximize the rate of the change of its energy).

The solution of the considered minimum-time version of the Earth-Mars problem aligns with an ephemeris-consistent rendezvous boundary conditions (i.e., the position and velocity of Mars depend on the time of flight). The resulting minimum-time trajectory can be used to demonstrate the validity of the reachable set estimations because a minimum-time trajectory, by definition, must terminate on the reachable set. To show this, we compute the reachable position and velocity sets for the time of flight computed by the optimal single-trajectory indirect OCP [53]. Refer to Figure 5 that shows the evolution of the velocity reachable set through flight times from 120 to 180 days. We select these time of flights since they correspond to the thruster direction reversing in Figure 4. The reachable set appears to fold upon itself when chronologically stepping from 140 days (Fig. 5b) to 160 days (Fig. 5c). This shows that the behaviors of the reachable position and velocity sets are not obviously correlated.

The reachable set algorithm was used to compute the reachable set for a time horizon of 307 days with 5000 sample points. Figure 6a shows the position reachable set for the given initial conditions. Upon examination, we see that the indirect OCP generates a position-feasible trajectory (green line) due to the fact that in position-space, the minimum-time trajectory terminates on the interior of the projected position reachable set. Figure 6b depicts the velocity reachable set. The indirect minimum-time trajectory terminates on the boundary of the velocity reachable set. This indicates that for the considered parameters of the propulsion system the velocity states are more restrictive, compared to the position set, and reduces the combined reachable velocity. Moreover, the results are consistent and validates the accuracy of the method for determining an accurate estimate of reachable set for low-thrust spacecraft. However, the sensitivity of the

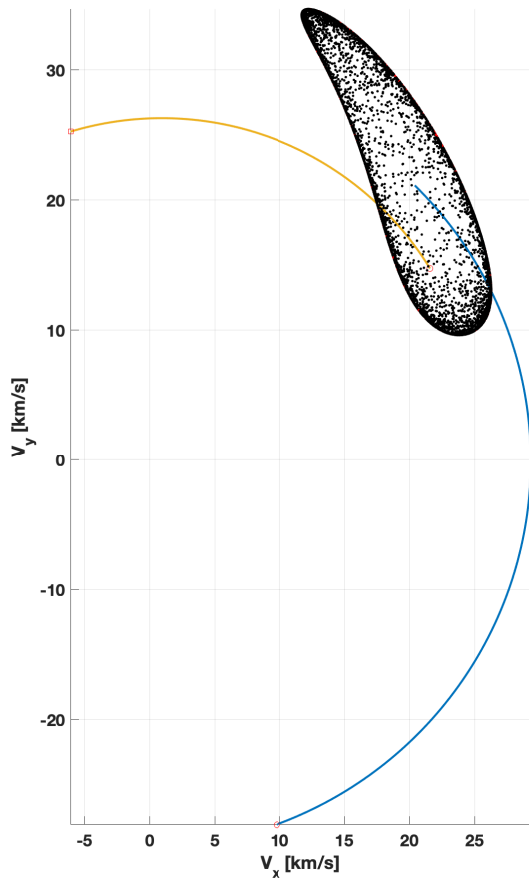


(a) Minimum-time trajectory and thrust vector.

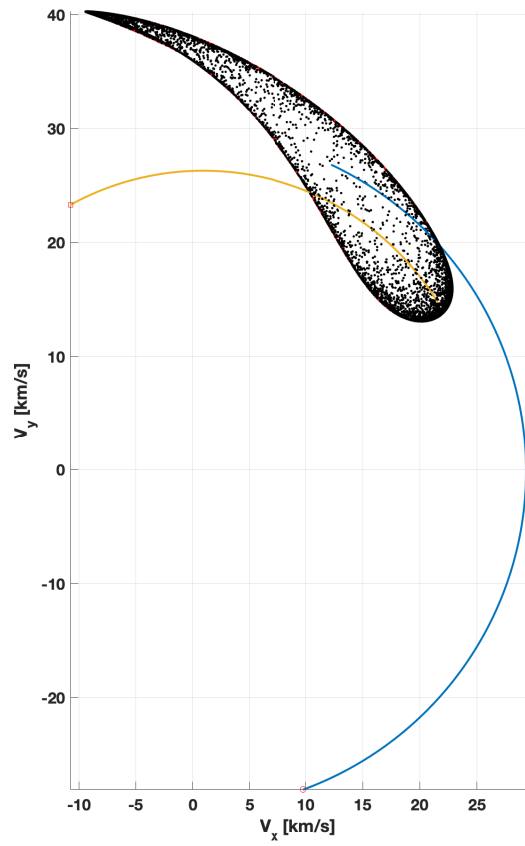


(b) Components of the control vector.

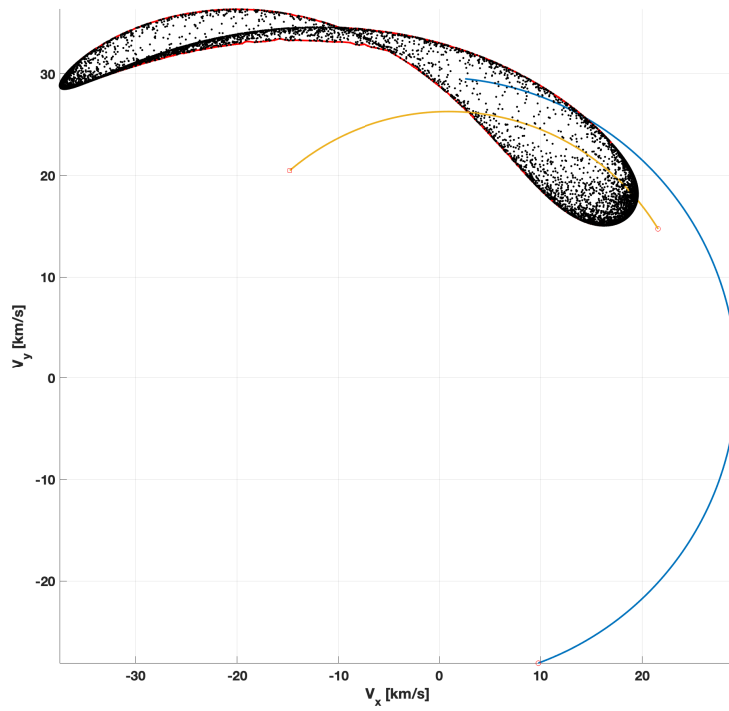
Fig. 4 Minimum-time Earth-Mars problem solved with CasADi.



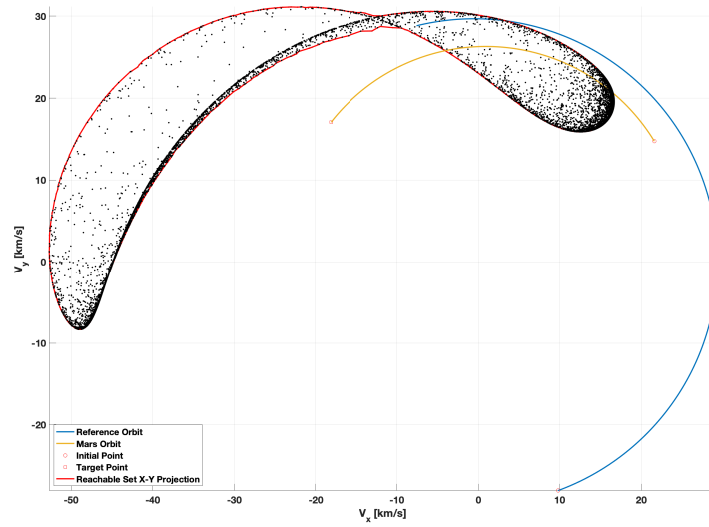
(a) 120 Days.



(b) 140 Days.

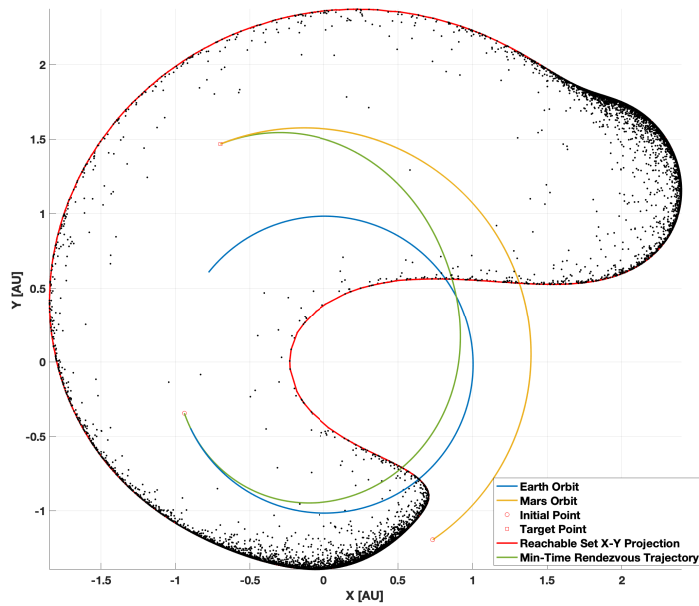


(c) 160 Days.

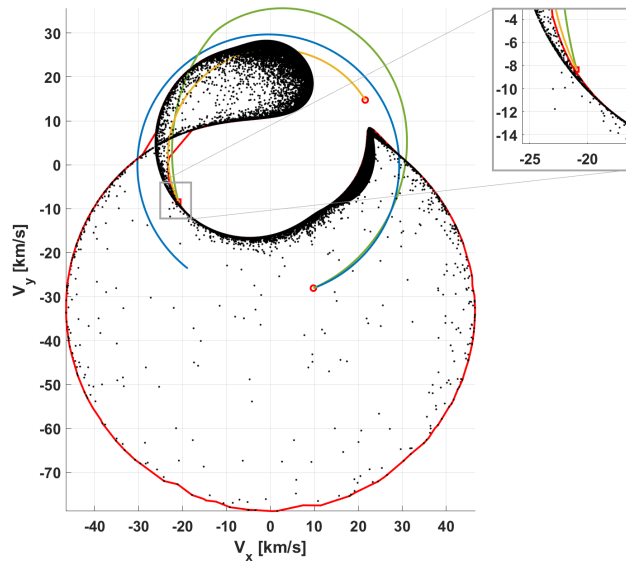


(d) 180 Days.

**Fig 5 Evolution of reachable velocity set vs. different time horizons.**



(a) Position reachable set.



(b) Velocity reachable set.

**Fig. 6** Reachable set over a 307-day time horizon with 5000 sample trajectories and minimum-time trajectory.

reachable set for fixed-time rendezvous maneuvers is more nuanced, as is discussed for a rendezvous maneuver from Earth to asteroid 1989ML in [48], which is a consequence of the deformed reachable set with the orbit of Mars.

### C. Reachable set propagation and analysis of the computation time

One useful application of this reachable set determination method is the ability to rapidly determine if a planet/object can be encountered from given initial conditions in a specified time horizon. To demonstrate this capability, the reachable set algorithm was initialized such that one stage is equal to one day. Then, 10,000 sample trajectories are computed for each trial. Data indicating the time of flight and simulation run times are presented in Table 1. The fast computation time allows for rapid iteration to “brute force” search for a time of flight that allows a target to become reachable.

**Table 1 Earth-Mars reachable set propagation with 10,000 sample points.**

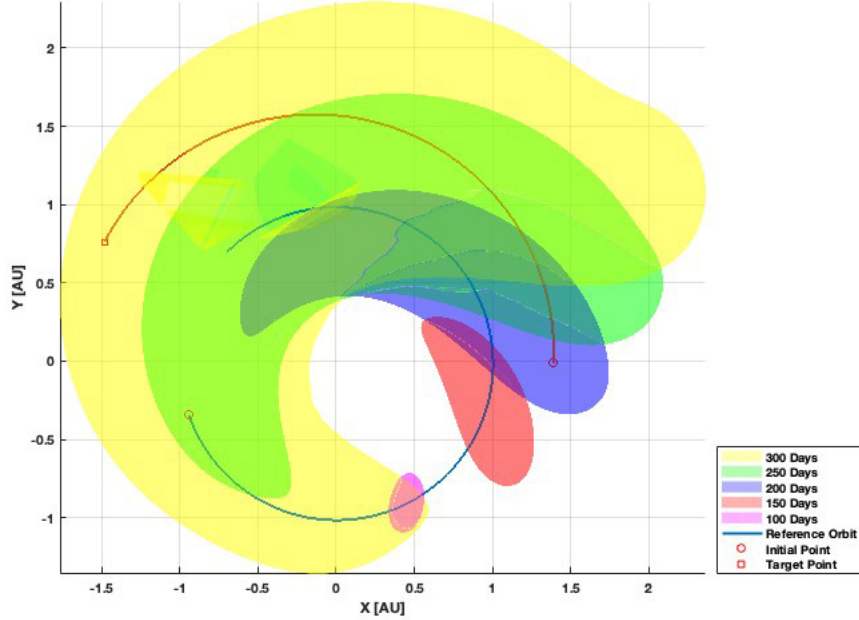
Time of Flight (days)	Computation time (seconds)
100	9.0599
150	17.3945
200	18.1148
250	21.8414
300	26.2118

Figure 7 indicates the expansion of the reachable position set through an increasing time horizon. This pseud-qualitative plot was generated by interpolating all sampled trajectories on the reachable set to graphically illustrate the reachable set. The reachable set algorithm was run five times, with flight times ranging from 100 to 300 days. The trajectory of Mars (red line) shows how the target position evolves with increasing time of flight. The power of the rapid reachable algorithm is illustrated here, since the successive generation of many reachable sets for complex problems is extremely computationally expensive. From Figure 7 we can see that time of flight must be greater than 250 days for Mars to be reachable. Recall that position-reachability is the first step in determining if an object can be reached if a rendezvous scenario is of interest, which confirms the results of the previous section.

### D. Reachable set variations with uncertainties in initial boundary conditions

We revisit the simulation presented in Section IV.A to demonstrate the ability to add uncertainties in initial boundary conditions and to assess the impact of them on the reachable set. Two types of initial boundary conditions are considered: 1) position and velocity uncertainty, and 2) an impulse maneuver. Both types of constraints can be incorporated simultaneously, however, we separate them in these results to demonstrate their individual effects. We consider departure from the Earth (reference) orbit.

Figure 8a shows the reachable set for a case without position and velocity uncertainty (green surface) and a case for ellipsoidal position and velocity (red surface). The addition of ellipsoidal uncertainty constraints clearly affects the nominal reachable set, in that it appears the red set had decreased in size relative to the green set. However, this is not necessarily the case since the uncertainty constraint has also shifted the red reachable set out of plane relative to the green reachable set, making it appear smaller. The main conclusion is the demonstration that ellipsoidal uncertainty

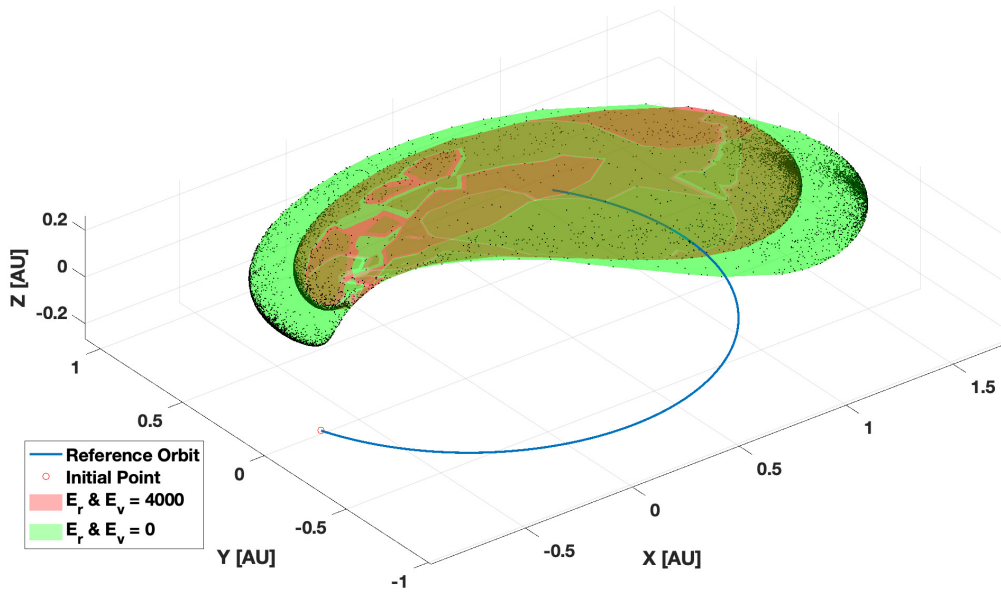


**Fig. 7 Depiction of the Earth-Mars low-thrust position-level of the reachable set.**

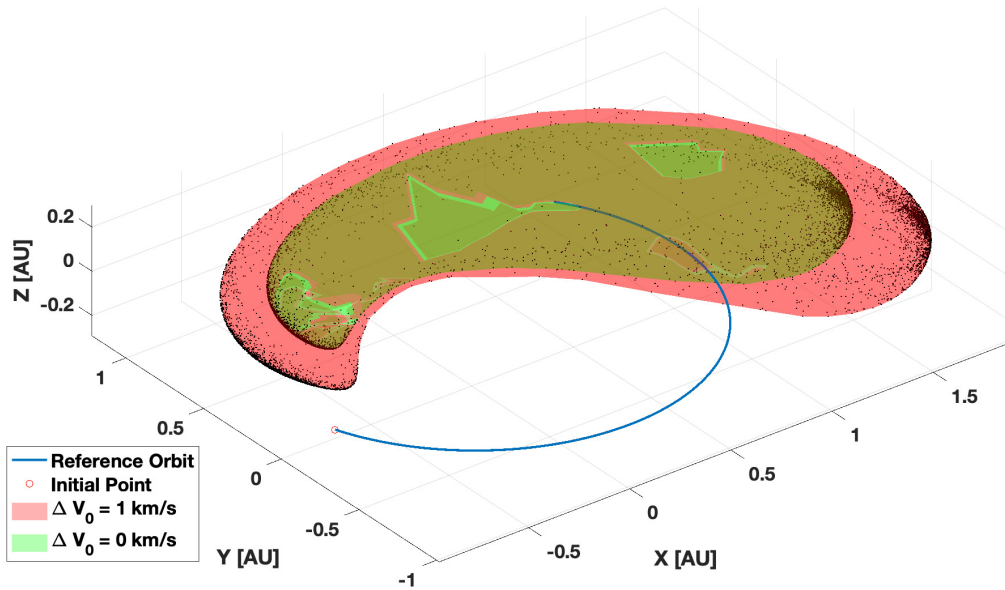
constraints can significantly affect the reachable set. Figure 8b presents the expected result of adding an initial  $\Delta V$  impulse (which can be considered as excess velocity provided by a launch vehicle). The impulse maneuver excites the spacecraft to a higher energy state, which ultimately leads to a larger reachable set. The red set of the impulse maneuver, is noticeably expanded after a 200-day time interval compared to the zero-impulse maneuver reachable set (green color).

## V. CR3BP Reachable Set Results

Results are presented for three cases by considering different spacecraft parameters over various time horizon values to showcase the versatility of the proposed algorithm and to reveal the characteristics of the resulting reachable sets. Case 1 is an L1 point initial condition with no velocity over increasing time horizon values and is in agreement with results presented in [62]. Case 2 simulates an L2 Halo orbit over both short- and long-time-horizon values and illustrates the chaotic natural dynamics and reachable set evolution of the CR3BP. Case 3 updates the initial condition to a 9:2 NRHO, which is the chosen orbit for NASA's Lunar Gateway station [63]. Case 1 serves to validate the reachable set results, whereas Cases 2 and 3 present novel reachable set solutions in cislunar space. Last, a theoretical explanation involving invariant manifolds is presented to offer additional insights into the evolution of the reachable set in the CR3BP. In all results presented, the Earth and Moon are not illustrated to scale and the segment duration,  $\Delta t$ , was determined empirically as the time of flight normalized by characteristic time divided by 200.



(a) With uncertainties on the initial position and velocity vectors (per definition given in Eq. (19)).



(b) With an initial impulse maneuver (per definitions given in Eqs. (25) and (26)).

Fig. 8 Reachable sets over a 200-day time horizon with 5000 samples with different initial types of uncertainties.

### A. L1 Point reachability

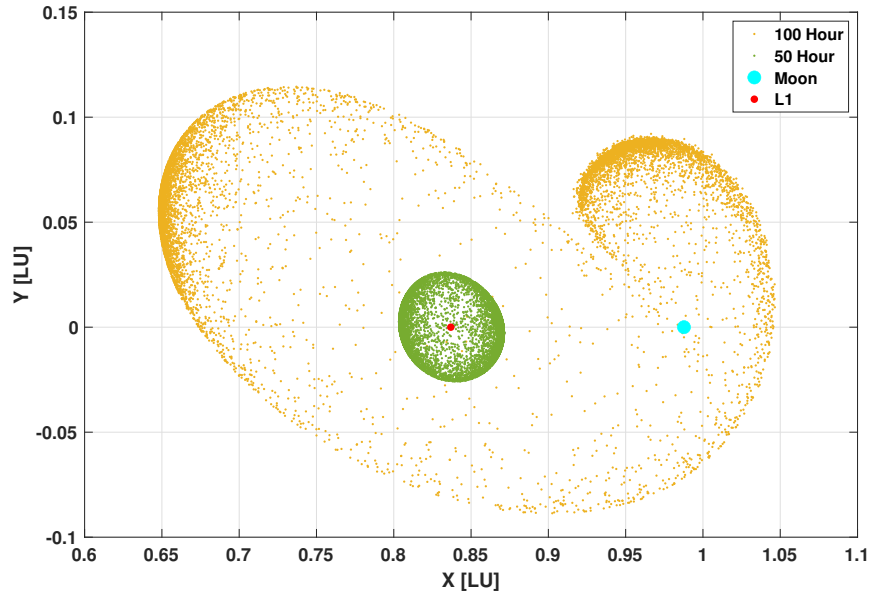
A low-thrust spacecraft with  $T_{\max} = 1$  Newton,  $I_{\text{sp}} = 2000$  seconds, and 1500 kg of initial mass is considered. The initial state vector is given in nondimensionalized coordinates as  $\mathbf{x} = [0.836892919; 0; 0; 0; 0; 0]^T$ . The reachable set was computed for times of flight ranging from 50 to 200 hours. Each trial uses 100,000 sample trajectories. The longest simulation run time, for 200 hours, took 119 seconds. Comparing with [62], which is a planar implementation of cislunar CR3BP, Figure 9 utilizes full three-dimensional dynamics. The sample points that lie on the interior of the reachable set with this  $X - Y$  projection are due to the out-of-plane effects and are simply reachable points with a  $Z$ -coordinate not equal to zero. The results validate the accuracy of the linearization of the CR3BP dynamics.

### B. L2 Halo orbit reachability

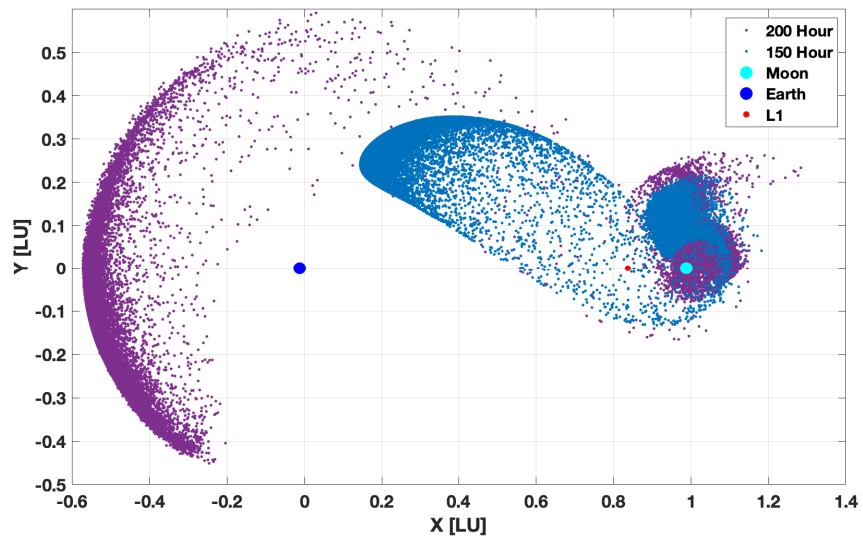
Case 2 considers computation of the reachable set for a L2 Halo Orbit. A low-thrust spacecraft with  $T_{\max} = 0.2$  Newton,  $I_{\text{sp}} = 3000$  seconds, and  $m_0 = 1000$  kg is considered. The initial state vector is given in nondimensionalized coordinates as  $\mathbf{x} = [1.17204419281306; 0; -0.0862093101977581; 0; -0.188009087163036; 0]^T$ . The period of the L2 reference orbit is 346.322857 hours. The 3D trajectory encounters significant multi-body effects. The reachable set was computed for times of flight of 150 and 350 hours. The 150-hour time horizon demonstrates the evolution of the reachable set in the vicinity of the moon, and the 350-hour trial shows growth and a disjoint reachable set.

Figure 10 shows the 150 hours expansion of the reachable set for a low-thrust spacecraft under CR3BP dynamics with 2,000 sample trajectories. Even on this short time horizon, one can identify that small changes in the thrust vector (especially during initial stages) directly contribute to a reachable set that is fully integrated in three dimensions. Unlike the two-body results (see Figs. 3, 6, and 8) in which it is straightforward to interpolate the reachable sample points to generate a reachable set boundary projection, it is very difficult to accomplish with the abstract reachable set shape that is illustrated here. Additionally, Figure 10 shows an incipient tendency for the reachable trajectories to cluster into two bands, each propagating in opposite directions from the initial point. This phenomenon is the primary purpose of including the relatively long 350-hour time horizon case and will be explained in the section on invariant manifolds.

For the 350-hour test case, the number of sample points was increased to 10,000 to increase the resolution of the captured reachable set. Figure 11 presents the computed reachable set for the L2 Halo reference orbit. These results show clearly that the reachable set has disconnected into two primary clusters. One cluster completes a close fly-by with the moon and the second cluster exits the near vicinity of the moon into an area dominated by the gravitational attraction of the Earth. The section detailing invariant manifolds will outline the theoretical foundation for why this reachable set is disjoint and why the uniformly sampled trajectories are exhibiting unexpected clustering behavior.

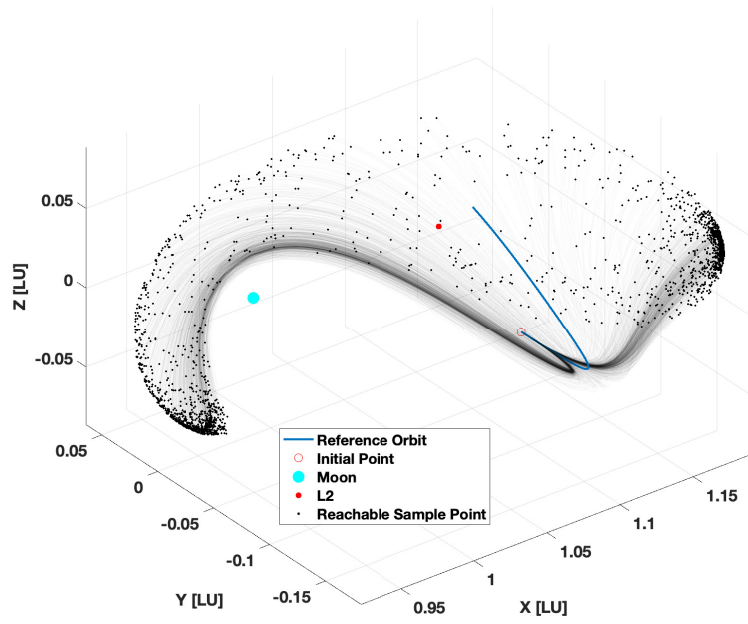


(a) 50-100 Hour Time of Flight

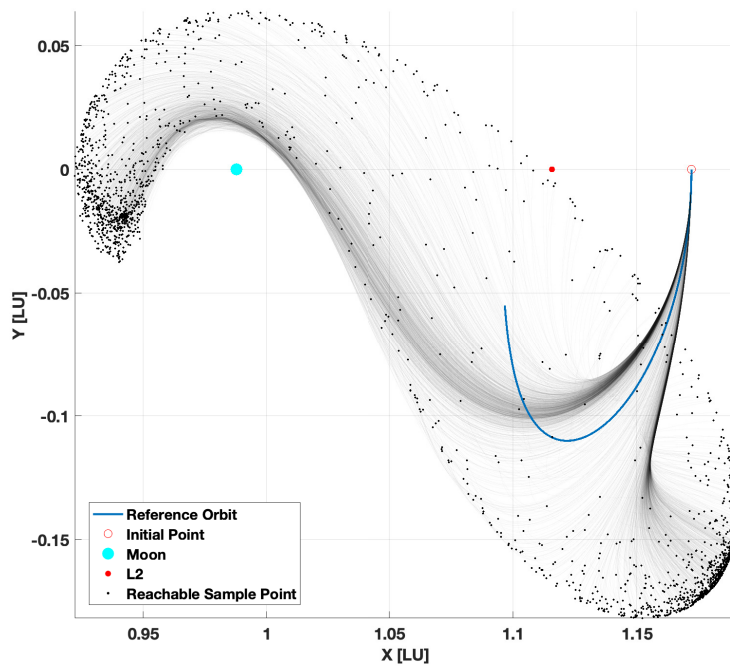


(b) 150-200 hour time of flight.

**Fig. 9** L1 Point reachable sets with increasing time of flight.

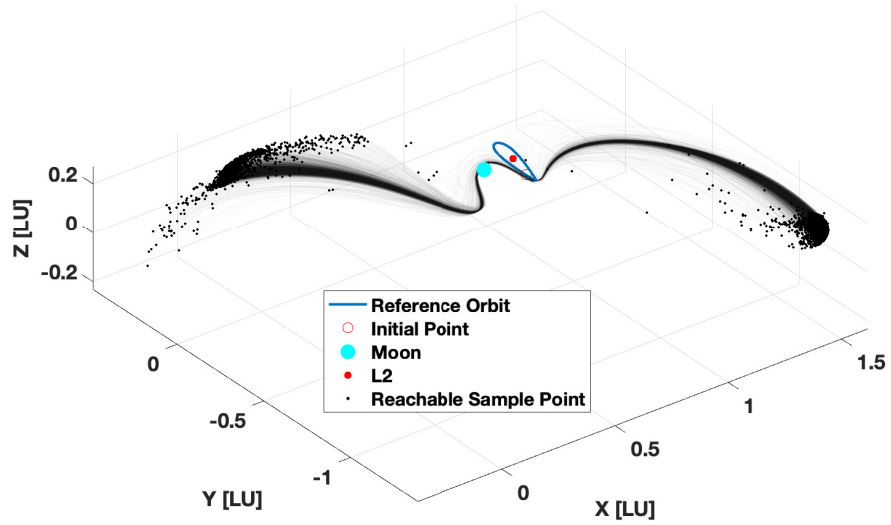


(a) 3D view.

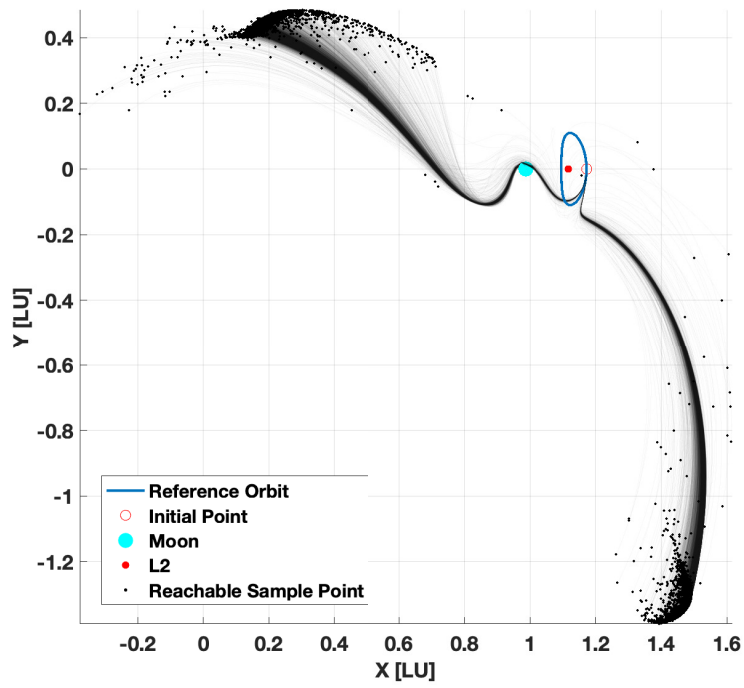


(b) XY view.

Fig. 10 Position reachable set over a 150-hour (6.25 days) time horizon with 2000 sample trajectories.



(a) 3D view.



(b) XY view.

Fig. 11 Position reachable set over a 350-hour time horizon with 10,000 sample trajectories.

### C. 9:2 NRHO reachability

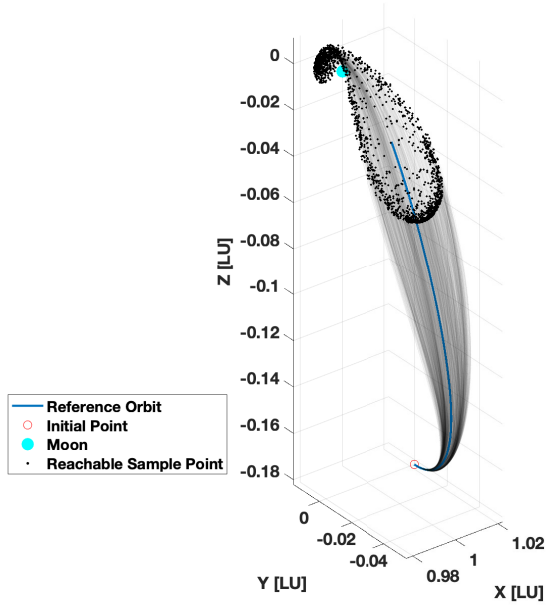
Case 3 considers the reachable set for the Lunar Gateway earmarked 9:2 NRHO. A low-thrust spacecraft with  $T_{\max} = 0.2$  Newton,  $I_{\text{sp}} = 3000$  seconds and  $m_0 = 1000$  kg is used. The initial state vector is given in nondimensionalized coordinates as  $\mathbf{x} = [1.0221, 0, -0.1821, 0, -0.1033, 0]^T$  [57]. The period of the L2 reference orbit is 157.500622 hours. All results are computed with a 75-hour time of flight and 2,000 sample trajectories. The region in the vicinity of the 9:2 NRHO will become a congested area in the near future, so it is imperative to be able to compute reachable sets to perform accurate spacecraft proximity operations in this space and execute potential collision-avoidance maneuvers.

Figure 12 presents the computed reachable set for the 9:2 NRHO over 75 hour time of flight with 2,000 sample trajectories. This result shows a new characteristic of the reachable set, that is, the reachable set not only expands, but also contracts with this time horizon. Before the spacecraft reaches the perilune of the 9:2 NRHO reference orbit, the reachable set expands in a manner consistent with previous results. At perilune, the natural CR3BP dynamics contract the reachable set before expanding again after perilune.

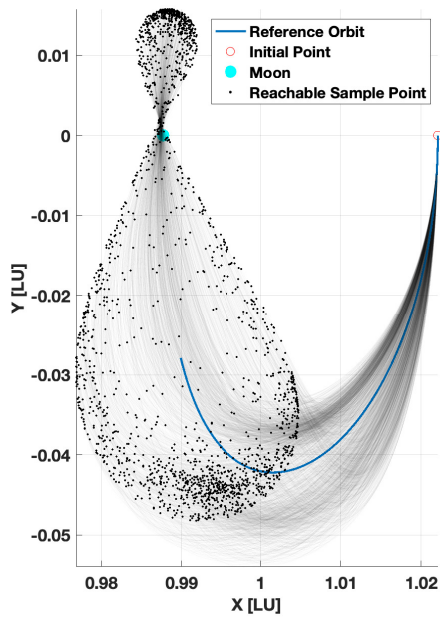
### D. Connection between reachable sets and invariant manifolds in CR3BP

Historically, low-energy transfers in three-body dynamical models originated with the idea of invariant manifolds. These dynamical structures exist in the vicinity of the three-body libration points and can be used to connect trajectories across vast distances in space [64]. An observation from the results presented for a low-thrust spacecraft in the CR3BP exhibits an interesting behavior over long time horizons, namely, the reachable set exhibits a bifurcation (i.e. there exist “two” different directions leading to reachable sets starting from the same initial condition). Additionally, when all the sampled minimum-time trajectories are plotted, they appear to be clustering around some unknown dynamical structure in the CR3BP. Examining the structure of the presented algorithm, the terminal costates are sampled from a uniformly distributed ball, which follows that the reconstructed thrust vector should also reflect the uniform sampling. This is not consistent with the observations, in that there appear some thrust vectors that are, broadly, “more likely” due to the chaotic nature of the CR3BP. We will now attempt to explain this phenomenon of a disjoint reachable set and the clustering of sampled trajectories.

We briefly digress to a discussion from Chaos Theory and the bifurcation of the logistic map. The original 1967 paper from May [65] details how chaos emerges from the iterative solution to the logistic difference equation when the growth rate exceeds 3.570. In detailed plots of the logistic map, examining the regions beyond 3.570 with an unstable fixed point, there appear to be some “more” stable points that appear as peaks of a probability distribution in the chaotic region. These are referred to as supertracks (ST) [66]. Returning to the analysis of the reachable sets in the CR3BP, we hypothesize that the clustering of sampled reachable trajectories is analogous to ST’s of the logistic map. The CR3BP is a chaotic system similar to the logistic map in that there exist stable manifolds and libration points. We ascertain that the clustering of sample trajectories is coincident with the invariant manifolds that exist as quasi-stable/unstable structures



(a) 3D view.



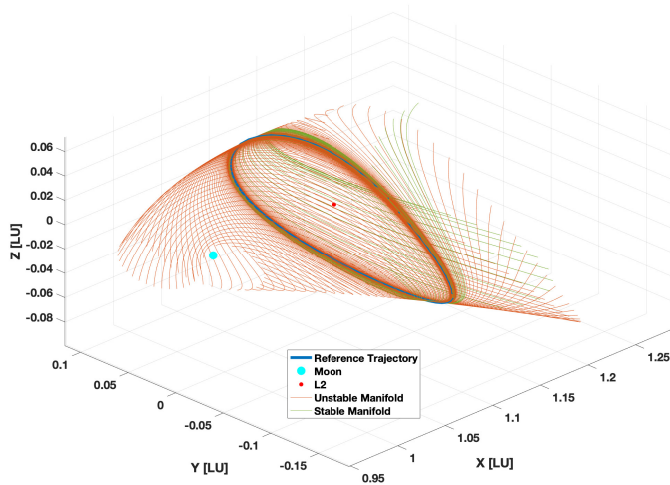
(b) XY view.

Fig. 12 Position reachable set over a 75-hour time horizon with 2,000 sample trajectories.

in the CR3BP. To empirically validate our hypothesis, invariant manifolds associated with the considered L2 Halo orbit will be computed. These invariant manifolds will be overlaid on the results from the reachable set analysis.

Invariant manifolds are computed according to the process outlined in [67] and [68] and is straightforward to construct by the IMF. Beginning with the reference periodic orbit, we can compute the Monodromy matrix,  $M(t_0)$ , through a numerical integration of the state transition matrix,  $\Phi$  (using Eq. (7) with  $\mathbf{u} = \mathbf{0}$ ) from an initial point for one orbital period,  $T$ , as  $M(t_0) = \Phi(t_0 + T, t_0)$ . Different selections of the initial point on the periodic orbit will yield different  $M(t_0)$ , which is useful for reconstructing the complete invariant manifolds. Next, compute the eigenvalues of  $M(t_0)$ . For Halo orbits, the six eigenvalues are  $\lambda_1 = 1/\lambda_2$ ,  $\lambda_3 = \lambda_4 = 1$ ,  $\lambda_5 = \lambda_6^*$ , where  $\lambda_1$  and  $\lambda_2$  are the real unstable and stable eigenvalues, respectively. In fact,  $\lambda_3$  and  $\lambda_4$  indicate neutral stability and  $\lambda_5$  and  $\lambda_6^*$  are a complex conjugate pair that lie on the unit circle and contribute only to rotation (i.e. neutrally stable directions). Extracting the eigenvectors associated with the unstable and stable eigenvalues allows for a perturbation in the unstable or stable direction on the initial condition as,  $\mathbf{x}_U(t_0) = \mathbf{x}(t_0) + s\epsilon\xi_{U,0}$ , and  $\mathbf{x}_S(t_0) = \mathbf{x}(t_0) + s\epsilon\xi_{S,0}$  where  $\xi_{U,0}$  and  $\xi_{S,0}$  are the unstable/stable eigenvector,  $s = \pm 1$  indicates the direction of the manifold, and  $\epsilon$  is a small offset. These perturbed initial conditions can be numerically integrated to recover the unstable and stable manifolds in both the forward and backward directions by selecting different values for  $s$ . Selecting different  $\mathbf{x}(t_0)$  along the period orbit, recomputing the Monodromy matrix and using and integrating along stable and unstable eigenvalues will yield an approximation of the invariant manifolds associated with a designated periodic orbit (see Fig. 13). Invariant manifolds associated with the reference L2 Halo orbit are computed for a short time horizon are shown below. The motivation of this brief discussion on invariant manifolds was to explain the disjoint reachable set and reachable sample trajectory clustering most directly observed in Figure 11. The unstable and stable manifolds are computed for this same L2 Halo reference periodic orbit and then overlaid onto the reachable set results from Figure 11 to identify a possible trend in reachable trajectories arising from any underlying dynamical structure associated with the chosen periodic orbit.

Figure 14 presents the L2 Halo 350-hour reachable set with the associated invariant manifolds. There is a clear direct relationship, for this long time horizon, of the tendency for reachable set sample trajectories to cluster on the invariant manifolds. Identify that the invariant manifolds propagate in two primary directions originating at the periodic orbit, which is due to the integration in both the forward and backward directions due to variations in the parameter,  $s$  [68]. Since the reachable set is, by definition, the set of all possible states that could be achieved from a given initial condition, it is expected that the sample points terminating the furthest linear distance from the initial condition arrived at the terminal point by exploiting the invariant manifold structure existing in the CR3BP. Additionally, since the propulsion system used for this model (0.2 Newtons) is very low leading to an overall small perturbation acceleration, it is expected that the reachable set evolution on this time horizon is dominated more by the dynamics in the CR3BP than the on-board propulsion system. That is, there is a higher probability of a reachable sample point to terminate near an invariant manifold than any other random spatial coordinate, making these invariant manifolds essentially analogous to



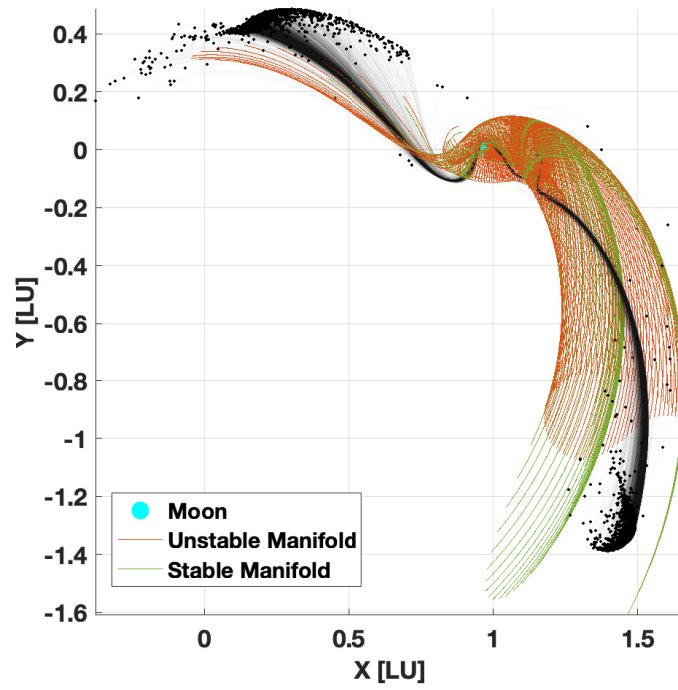
**Fig. 13** Stable and unstable invariant manifolds of the Earth-Moon L2 Halo Orbit.

supertracks in a general chaotic dynamical system. To our best knowledge, the relation between the reachable set of low-thrust trajectories and invariant manifolds in the CR3BP is not identified in the literature.

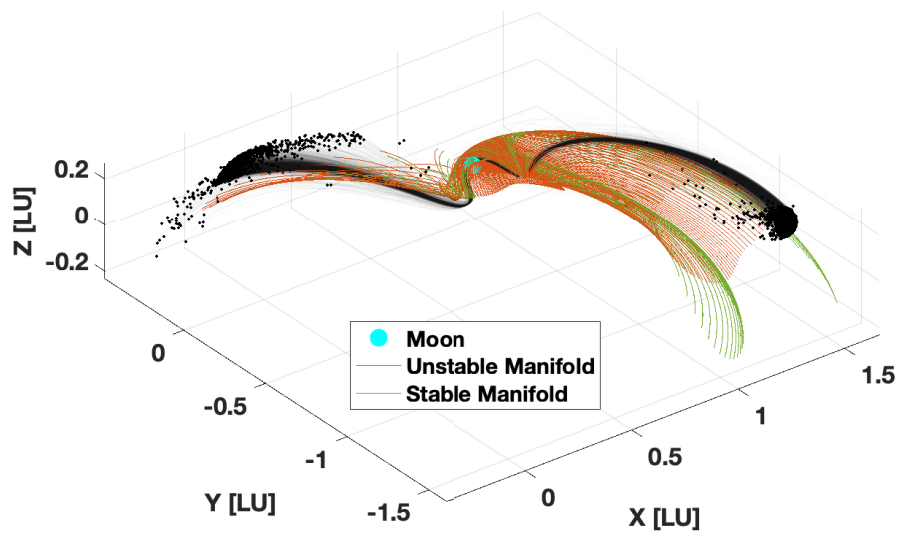
## VI. Conclusion

The indirect multistage formulation of optimal control theory was used to implement a rapid reachable set approximation algorithm. A minimum-time low-thrust trajectory formulation was used to recover minimum-time trajectories corresponding to reachable sets. Results are presented detailing the application of this algorithm to a minimum-time Earth-Mars transfer. Results indicate that the minimum-time rendezvous lies on the interior of the reachable position set and on the boundary of the reachable velocity set. The effects of injecting initial condition uncertainty and an impulsive maneuver are also evaluated, which shows variations in the reachable set. Novel results detailing the reachable set for low-thrust CR3BP dynamics are presented for L1 point, L2 Halo, and 9:2 NRHO reference conditions were analyzed. Finally, theoretical insight into the behavior of the reachable set, subject to multi-body perturbations, is provided to show that the reachable set and the invariant manifold structures closely align.

The two situations where the proposed algorithm demonstrates areas for improvement are when a reachable set passes close to a gravitational body and in a multi-revolution scenario. For the former, when we observe the reachable set to develop to encompass a gravitational body, the resulting reachable set appears chaotic. The latter is an extension of the long time horizon shortcoming in that for a multi-revolution case the reachable set will overlap with itself and the set becomes incoherent. Our results also indicate that thrust-reversal maneuvers also deform the velocity reachable set. In general, these shortcomings can be avoided completely by computing short time horizon reachable sets, which is the most likely application for a space-domain awareness situation.



(a) 3D view



(b) XY view

Fig. 14 350-hour L2 reference orbit reachable set overlaid with invariant manifolds.

## VII. Appendix: Derivation of Boundary Conditions for An Initial Impulse Maneuver

An initial impulsive maneuver introduces the constraint given in Eq. (24). The augmented Hamiltonian is formed as,

$$H^* = m_0 - m_0 e^{-\frac{\Delta V}{c}} + \lambda^\top \left[ \mathbf{r}^{*\top}, \mathbf{v}^{*\top} \right]^\top + \nu_3 \left( \frac{1}{2} \delta \mathbf{v}_2^\top \delta \mathbf{v}_2 - \frac{1}{2} \Delta V_{\max}^2 \right). \quad (27)$$

We can explicitly define the relationship between  $\delta \mathbf{v}_2$  and  $\Delta V$  as  $\Delta V = \|\delta \mathbf{v}_2\| = \sqrt{\delta \mathbf{v}_2^\top \delta \mathbf{v}_2}$ . Additionally, the derivative of  $\Delta V$  with respect to  $\delta \mathbf{v}_2$  is found as the derivative of a 2-norm function given by,

$$\frac{\partial \Delta V}{\partial \delta \mathbf{v}_2} = \frac{\partial \|\delta \mathbf{v}_2\|}{\partial \delta \mathbf{v}_2} = \frac{\delta \mathbf{v}_2}{\|\delta \mathbf{v}_2\|} = \frac{\delta \mathbf{v}_2}{\Delta V}. \quad (28)$$

Forming the necessary conditions for optimality, we obtain,

$$\frac{\partial H^*}{\partial \delta \mathbf{v}_2} = H_{\delta \mathbf{v}_2}^* = \mathbf{0} = \lambda_{\mathbf{v}_2} + \frac{\delta \mathbf{v}_2}{\Delta V} \frac{m_0}{c} e^{-\frac{\Delta V}{c}} + \nu_3 \delta \mathbf{v}_2. \quad (29)$$

Since Eq. 24 is an inequality, the solution process is to assume the constraint is active by setting  $\Delta V = \Delta V_{\max}$ , obtain an expression for  $\nu_3$ , and check if  $\nu_3 > 0$ . If the inequality is inactive, we will set  $\nu_3 = 0$  to solve for an expression for  $\Delta V$ . Applying this logic and substituting into the right relation in Eq. 29, we obtain,

$$\lambda_{\mathbf{v}_2} = - \left( \frac{m_0}{\Delta V_{\max} c} e^{-\frac{\Delta V_{\max}}{c}} + \nu_3 \right) \delta \mathbf{v}_2. \quad (30)$$

In order for the equality condition in Eq. 30 to be satisfied,  $\lambda_{\mathbf{v}_2}$  must be parallel to  $\delta \mathbf{v}_2$ . Hence, the optimal solution for  $\delta \mathbf{v}_2$  when the inequality constraint is binding can be determined from Lawden's Primer Vector theory as,

$$\delta \mathbf{v}_2 = -\Delta V_{\max} \frac{\lambda_{\mathbf{v}_2}}{\|\lambda_{\mathbf{v}_2}\|}, \rightarrow \delta \mathbf{v}_2 + \Delta V_{\max} \frac{\lambda_{\mathbf{v}_2}}{\|\lambda_{\mathbf{v}_2}\|} = \mathbf{0}, \rightarrow \lambda_{\mathbf{v}_2} + \frac{\|\lambda_{\mathbf{v}_2}\|}{\Delta V_{\max}} \delta \mathbf{v}_2 = \mathbf{0}. \quad (31)$$

Setting the term in parentheses in Eq. (30) to  $\|\lambda_{\mathbf{v}_2}\| / \Delta V_{\max}$ ,

$$\frac{\|\lambda_{\mathbf{v}_2}\|}{\Delta V_{\max}} = \frac{m_0}{\Delta V_{\max} c} e^{-\frac{\Delta V_{\max}}{c}} + \nu_3, \rightarrow \nu_3 = \frac{\|\lambda_{\mathbf{v}_2}\|}{\Delta V_{\max}} - \frac{m_0}{\Delta V_{\max} c} e^{-\frac{\Delta V_{\max}}{c}} > 0. \quad (32)$$

Only the sign of  $\nu_3$  is required, so Eq. (32) can be simplified by multiplying all terms by  $\Delta V_{\max} m_0 c e^{-\frac{\Delta V_{\max}}{c}}$ .

$$\nu_3 = \|\lambda_{\mathbf{v}_2}\| m_0 c e^{-\frac{\Delta V_{\max}}{c}} - \left( m_0 e^{-\frac{\Delta V_{\max}}{c}} \right)^2 > 0. \quad (33)$$

Equation (33) can be evaluated for each of the sample trajectories in a problem to determine if  $\nu_3 > 0$ . If true, Eq. (31) is the optimal solution for  $\delta \mathbf{v}_2$  and  $\Delta V = \Delta V_{\max}$ . If false, then  $\Delta V \neq \Delta V_{\max}$ , set  $\nu_3 = 0$  and solve Eq. (30) for

$\Delta V$ . Equation (30) with updated notation for a non-binding inequality constraint and  $v_3 = 0$  is

$$\mathbf{0} = \lambda_{v_2} - \left( \frac{m_0}{\Delta V c} e^{-\frac{\Delta V}{c}} \right) \delta v_2, \rightarrow \mathbf{0} = \lambda_{v_2} - \left( \frac{m_0}{c} e^{-\frac{\Delta V}{c}} \right) \frac{\delta v_2}{\Delta V}. \quad (34)$$

We have factored  $\Delta V$ , since it is related to  $\delta v_2$  by  $\Delta V = \|\delta v_2\|$ . Similar to the constraint binding case, notice that  $\lambda_{v_2}$  must be parallel to  $\frac{\delta v_2}{\Delta V}$  to satisfy Equation 34. That is,

$$\frac{\delta v_2}{\Delta V} = \frac{\lambda_{v_2}}{\|\lambda_{v_2}\|}. \quad (35)$$

The term in parentheses in Equation 34 must equal  $\|\lambda_{v_2}\|$ , which can be written as,

$$\|\lambda_{v_2}\| = \frac{m_0}{c} e^{-\frac{\Delta V}{c}}, \rightarrow 0 = \frac{m_0}{c} e^{-\frac{\Delta V}{c}} - \|\lambda_{v_2}\|. \quad (36)$$

Multiplying by  $m_0 c e^{-\frac{\Delta V}{c}}$  to simplify and solve the resulting quadratic equation for  $m_0 e^{-\frac{\Delta V}{c}}$

$$0 = \left( m_0 e^{-\frac{\Delta V}{c}} \right)^2 - \|\lambda_{v_2}\| c \left( m_0 e^{-\frac{\Delta V}{c}} \right), \rightarrow m_0 e^{-\frac{\Delta V}{c}} = \frac{\|\lambda_{v_2}\| c \pm \sqrt{\|\lambda_{v_2}\|^2 c^2}}{2}. \quad (37)$$

To minimize fuel (i.e., maximize the left-hand side of Eq. 37), the positive sign has to be selected to have

$$\Delta V = -c \ln \left( \frac{\|\lambda_v\| c + \sqrt{\|\lambda_v\|^2 c^2}}{2m_0} \right), \quad (38)$$

This  $\Delta V$  can be used to recover  $\delta_n$ . The perturbation on initial conditions due to an impulsive maneuver is given by substituting Eq. (38) into the primer vector in Eq. (31),

$$\delta v_2 = c \ln \left( \frac{\|\lambda_v\| c + \sqrt{\|\lambda_v\|^2 c^2}}{2m_0} \right) \frac{\lambda_v}{\|\lambda_v\|}. \quad (39)$$

## VIII. Disclaimer

The first author would like to emphasize that the views expressed in this article are those of the authors and do not reflect the official policy or position of the United States Air Force, Department of Defense, or the U.S. Government.

## IX. Acknowledgments

The authors would like to thank Dr. Prashant Patel for fruitful discussions about the indirect multistage formulation.

## References

- [1] Allen, R. E., Clark, A. A., Starek, J. A., and Pavone, M., “A machine learning approach for real-time reachability analysis,” *2014 IEEE/RSJ International Conference on Intelligent Robots and Systems*, IEEE, Chicago, IL, USA, 2014, pp. 2202–2208. <https://doi.org/10.1109/IROS.2014.6942859>.
- [2] “Space Prime - Spacwerx,” , Feb 2023. URL <https://spacwerx.us/space-prime/>.
- [3] Garcia, M., “Space debris and human spacecraft,” , Apr 2015. URL [https://www.nasa.gov/mission\\_pages/station/news/orbital\\_debris.html](https://www.nasa.gov/mission_pages/station/news/orbital_debris.html).
- [4] Liu, E., Yan, Y., and Yang, Y., “Analysis and determination of capture area for space debris removal based on reachable domain,” *Advances in Space Research*, Vol. 68, No. 3, 2021, pp. 1613–1626. <https://doi.org/10.1016/j.asr.2021.03.017>.
- [5] Vendl, J. K., and Holzinger, M. J., “Cislunar periodic orbit analysis for persistent space object detection capability,” *Journal of Spacecraft and Rockets*, Vol. 58, No. 4, 2021, pp. 1174–1185. <https://doi.org/https://doi.org/10.2514/1.A34909>.
- [6] Chen, Q., Qiao, D., and Wen, C., “Reachable Domain of Spacecraft After a Gravity-Assist Flyby,” *Journal of Guidance, Control, and Dynamics*, Vol. 42, No. 4, 2019, pp. 931–940. <https://doi.org/10.2514/1.G003576>.
- [7] “Overview | Mission - NASA’s Europa Clipper,” , Apr 2023. URL <https://europa.nasa.gov/mission/about/>.
- [8] Kirk, D. E., *Optimal control theory: an introduction*, Prentice-Hall networks series, Prentice-Hall, Englewood Cliffs, N.J, 1970.
- [9] Crandall, M. G., Evans, L. C., and Lions, P.-L., “Some properties of viscosity solutions of Hamilton-Jacobi equations,” *Transactions of the American Mathematical Society*, Vol. 282, No. 2, 1984, pp. 487–502. <https://doi.org/10.1090/S0002-9947-1984-0732102-X>.
- [10] Borrelli, F., Bemporad, A., and Morari, M., *Predictive Control for Linear and Hybrid Systems*., 1<sup>st</sup> ed., Cambridge University Press, 2017. <https://doi.org/10.1017/9781139061759>.
- [11] Trélat, E., “Optimal control and applications to aerospace: some results and challenges,” *Journal of Optimization Theory and Applications*, Vol. 154, 2012, pp. 713–758. <https://doi.org/10.1007/s10957-012-0050-5>.
- [12] Wallace, S. W. (ed.), *Applications of stochastic programming*, MPS-SIAM series on optimization, Society for Industrial and Applied Mathematics, Philadelphia, PA, 2005.
- [13] Chen, Q., Qiao, D., and Wen, C., “Minimum-Fuel Low-Thrust Trajectory Optimization via Reachability Analysis and Convex Programming,” *Journal of Guidance, Control, and Dynamics*, Vol. 44, No. 5, 2021, pp. 1036–1043. <https://doi.org/10.2514/1.G004766>.
- [14] Vinter, R., “A Characterization of the Reachable Set for Nonlinear Control Systems,” *SIAM Journal on Control and Optimization*, Vol. 18, No. 6, 1980, pp. 599–610. <https://doi.org/10.1137/0318044>.

- [15] Jiang, X., Xia, G., Feng, Z., Zheng, W. X., and Su, R., “Reachable Set Estimation of Multi-Agent Systems: An Approximate Consensus Perspective,” *IEEE Transactions on Control of Network Systems*, 2023, pp. 1–11. <https://doi.org/10.1109/TCNS.2023.3282131>.
- [16] Mitchell, I., Bayen, A., and Tomlin, C., “A time-dependent Hamilton-Jacobi formulation of reachable sets for continuous dynamic games,” *IEEE Transactions on Automatic Control*, Vol. 50, No. 7, 2005, pp. 947–957. <https://doi.org/10.1109/TAC.2005.851439>.
- [17] Girard, A., and Guernic, C. L., “Efficient Reachability Analysis for Linear Systems using Support Functions,” *IFAC Proceedings Volumes*, Vol. 41, No. 2, 2008, pp. 8966–8971. <https://doi.org/10.3182/20080706-5-KR-1001.01514>.
- [18] Asarin, E., Dang, T., and Girard, A., “Reachability Analysis of Nonlinear Systems Using Conservative Approximation,” *Hybrid Systems: Computation and Control*, Vol. 2623, edited by G. Goos, J. Hartmanis, J. Van Leeuwen, O. Maler, and A. Pnueli, Springer Berlin Heidelberg, Berlin, Heidelberg, 2003, pp. 20–35. [https://doi.org/10.1007/3-540-36580-X\\_5](https://doi.org/10.1007/3-540-36580-X_5), series Title: Lecture Notes in Computer Science.
- [19] Bansal, S., and Tomlin, C. J., “Deepreach: A deep learning approach to high-dimensional reachability,” *2021 IEEE International Conference on Robotics and Automation (ICRA)*, IEEE, 2021, pp. 1817–1824. <https://doi.org/10.1109/ICRA48506.2021.9561949>.
- [20] Xue, D., Li, J., Baoyin, H., and Jiang, F., “Reachable Domain for Spacecraft with a Single Impulse,” *Journal of Guidance, Control, and Dynamics*, Vol. 33, No. 3, 2010, pp. 934–942. <https://doi.org/10.2514/1.43963>.
- [21] Zhang, G., Cao, X., and Ma, G., “Reachable domain of spacecraft with a single tangent impulse considering trajectory safety,” *Acta Astronautica*, Vol. 91, 2013, pp. 228–236. <https://doi.org/10.1016/j.actaastro.2013.06.016>.
- [22] Chen, Q., Qiao, D., Shang, H., and Liu, X., “A new method for solving reachable domain of spacecraft with a single impulse,” *Acta Astronautica*, Vol. 145, 2018, pp. 153–164. <https://doi.org/10.1016/j.actaastro.2018.01.040>.
- [23] Duan, J., Liu, Y., and Ding, R., “Simple Method to Determine Reachable Domain of Spacecraft with a Single Impulse,” *Journal of Guidance, Control, and Dynamics*, Vol. 42, No. 1, 2019, pp. 168–174. <https://doi.org/10.2514/1.G003273>.
- [24] Wen, C., Zhao, Y., and Shi, P., “Precise Determination of Reachable Domain for Spacecraft with Single Impulse,” *Journal of Guidance, Control, and Dynamics*, Vol. 37, No. 6, 2014, pp. 1767–1779. <https://doi.org/10.2514/1.G000583>.
- [25] Xuehua, L., Xingsuo, H., Qinfang, Z., and Ming, S., “Reachable domain for satellite with two kinds of thrust,” *Acta Astronautica*, Vol. 68, No. 11-12, 2011, pp. 1860–1864. <https://doi.org/10.1016/j.actaastro.2011.01.004>.
- [26] Vinh, N. X., Gilbert, E. G., Howe, R. M., Sheu, D., and Lu, P., “Reachable domain for interception at hyperbolic speeds,” *Acta Astronautica*, Vol. 35, No. 1, 1995, pp. 1–8. [https://doi.org/10.1016/0094-5765\(94\)00132-6](https://doi.org/10.1016/0094-5765(94)00132-6).
- [27] Wen, C., Zhao, Y., Shi, P., and Hao, Z., “Orbital Accessibility Problem for Spacecraft with a Single Impulse,” *Journal of Guidance, Control, and Dynamics*, Vol. 37, No. 4, 2014, pp. 1260–1271. <https://doi.org/10.2514/1.62629>.

- [28] Lu, L., Li, H., Zhou, W., and Liu, J., “Design and analysis of a direct transfer trajectory from a near rectilinear halo orbit to a low lunar orbit,” *Advances in Space Research*, Vol. 67, No. 3, 2021, pp. 1143–1154. <https://doi.org/10.1016/j.asr.2020.11.003>.
- [29] Wen, C., Sun, Y., Peng, C., and Qiao, D., “Reachable Domain Under J2 Perturbation for Satellites with a Single Impulse,” *Journal of Guidance, Control, and Dynamics*, Vol. 46, No. 1, 2023, pp. 64–79. <https://doi.org/10.2514/1.G006880>.
- [30] Wen, C., and Gao, Y., “Reachability Study for Spacecraft Maneuvering from a Distant Retrograde Orbit in the Earth-Moon System,” *AIAA18: 18th Australian International Aerospace Congress (2019): HUMS - 11th Defence Science and Technology (DST) International Conference on Health and Usage Monitoring (HUMS 2019): ISSFD - 27th International Symposium on Space Flight Dynamics (ISSFD)*, Engineers Australia, Royal Aeronautical Society., Melbourne, 2019, pp. 1666–1673.
- [31] Komendera, E., Scheeres, D., and Bradley, E., “Intelligent Computation of Reachability Sets for Space Missions,” *Proceedings of the AAAI Conference on Artificial Intelligence*, Vol. 26, No. 2, 2012, pp. 2299–2304. <https://doi.org/10.1609/aaai.v26i2.18973>.
- [32] Chernick, M., and D’Amico, S., “Closed-Form Optimal Impulsive Control of Spacecraft Formations Using Reachable Set Theory,” *Journal of Guidance, Control, and Dynamics*, Vol. 44, No. 1, 2021, pp. 25–44. <https://doi.org/10.2514/1.G005218>.
- [33] Xia, C., Zhang, G., and Geng, Y., “Reachable domain with a single coplanar impulse considering the target-visit constraint,” *Advances in Space Research*, Vol. 69, No. 10, 2022, pp. 3847–3855. <https://doi.org/10.1016/j.asr.2022.02.042>.
- [34] Lin, X., and Zhang, G., “Continuous-Thrust Reachable Set for Linear Relative Motion Near Elliptical Orbits,” *IEEE Transactions on Aerospace and Electronic Systems*, 2023, pp. 1–10. <https://doi.org/10.1109/TAES.2023.3313580>.
- [35] Pang, B., and Wen, C., “Reachable Set of Spacecraft With Finite Thrust Based on Grid Method,” *IEEE Transactions on Aerospace and Electronic Systems*, Vol. 58, No. 4, 2022, pp. 2720–2731. <https://doi.org/10.1109/TAES.2021.3138373>.
- [36] Lee, S., and Hwang, I., “Reachable set computation for spacecraft relative motion with energy-limited low-thrust,” *Aerospace Science and Technology*, Vol. 77, 2018, pp. 180–188. <https://doi.org/10.1016/j.ast.2018.02.034>.
- [37] Wang, Z., and Jiang, F., “Analytical Optimal Solution for the Reachable Domain of Low-Thrust Spacecraft,” *Journal of Spacecraft and Rockets*, 2023, pp. 1–11. <https://doi.org/10.2514/1.A35788>.
- [38] Surovik, D. A., and Scheeres, D. J., “Adaptive Reachability Analysis to Achieve Mission Objectives in Strongly Non-Keplerian Systems,” *Journal of Guidance, Control, and Dynamics*, Vol. 38, No. 3, 2015, pp. 468–477. <https://doi.org/10.2514/1.G000620>.
- [39] Wen, C., and Qiao, D., “Calculating collision probability for long-term satellite encounters through the reachable domain method,” *Astrodynamics*, Vol. 6, No. 2, 2022, pp. 141–159. <https://doi.org/10.1007/s42064-021-0119-8>.
- [40] Wu, C.-Y., and Russell, R. P., “Reachable Set of Low-Delta-v Trajectories Following a Gravity-Assist Flyby,” *Journal of Spacecraft and Rockets*, Vol. 60, No. 2, 2023, pp. 616–633. <https://doi.org/10.2514/1.A35464>.
- [41] Holzinger, M. J., Scheeres, D. J., and Erwin, R. S., “On-Orbit Operational Range Computation Using Gauss’s Variational Equations with J2 Perturbations,” *Journal of Guidance, Control, and Dynamics*, Vol. 37, No. 2, 2014, pp. 608–622. <https://doi.org/10.2514/1.53861>.

- [42] Holzinger, M. J., and Scheeres, D. J., “Reachability Results for Nonlinear Systems with Ellipsoidal Initial Sets,” *IEEE Transactions on Aerospace and Electronic Systems*, Vol. 48, No. 2, 2012, pp. 1583–1600. <https://doi.org/10.1109/TAES.2012.6178080>.
- [43] Kulumani, S., and Lee, T., “Systematic Design of Optimal Low-Thrust Transfers for the Three-Body Problem,” *The Journal of the Astronautical Sciences*, Vol. 66, No. 1, 2019, pp. 1–31. <https://doi.org/10.1007/s40295-018-00139-y>.
- [44] Bando, M., and Scheeres, D. J., “Nonlinear Attractive and Reachable Sets Under Optimal Control in Three-Body Problem,” *Journal of Guidance, Control, and Dynamics*, Vol. 41, No. 8, 2018, pp. 1766–1775. <https://doi.org/10.2514/1.G003334>.
- [45] Kousik, S., Vaskov, S., Bu, F., Johnson-Roberson, M., and Vasudevan, R., “Bridging the gap between safety and real-time performance in receding-horizon trajectory design for mobile robots,” *The International Journal of Robotics Research*, Vol. 39, No. 12, 2020, pp. 1419–1469. <https://doi.org/10.1177/0278364920943266>.
- [46] Kousik, S., Holmes, P., and Vasudevan, R., “Technical Report: Safe, Aggressive Quadrotor Flight via Reachability-based Trajectory Design,” , Jun. 2019. URL <http://arxiv.org/abs/1904.05728>, arXiv:1904.05728 [cs].
- [47] Bird, T. J., Pangborn, H. C., Jain, N., and Koeln, J. P., “Hybrid zonotopes: a new set representation for reachability analysis of mixed logical dynamical systems,” , Apr. 2023. URL <http://arxiv.org/abs/2106.14831>, arXiv:2106.14831 [cs, eess].
- [48] Taheri, E., and Junkins, J. L., “How Many Impulses Redux,” *The Journal of the Astronautical Sciences*, Vol. 67, No. 2, 2020, pp. 257–334. <https://doi.org/10.1007/s40295-019-00203-1>.
- [49] Patel, P. R., and Scheeres, D. J., “No Initial Guess Required: Rapidly Computing the Feasible Set of Fuel-Optimal Electric Propulsion Trajectories,” *33rd AAS/AIAA Space Flight Mechanics Meeting*, American Institute of Aeronautics and Astronautics, Austin, TX, 2023, pp. 1–21.
- [50] Patel, P. R., and Scheeres, D. J., “Rapidly and Automatically Estimating Reachability of Electric Propulsion Spacecraft,” *23rd Advanced Maui Optical and Space Surveillance Technologies Conference*, Maui, HI, 2022, pp. 1–15.
- [51] Bryson, A. E., and Ho, Y.-C., *Applied optimal control: optimization, estimation, and control*, rev. print ed., Cambridge University Press, Cambridge, 1975.
- [52] Bate, R. R., Mueller, D. D., and White, J. E., *Fundamentals of astrodynamics*, Dover Publications, New York, 1971.
- [53] Taheri, E., Li, N. I., and Kolmanovsky, I., “Co-state initialization for the minimum-time low-thrust trajectory optimization,” *Advances in Space Research*, Vol. 59, No. 9, 2017, pp. 2360–2373. <https://doi.org/10.1016/j.asr.2017.02.010>.
- [54] Junkins, J. L., and Taheri, E., “Exploration of Alternative State Vector Choices for Low-Thrust Trajectory Optimization,” *Journal of Guidance, Control, and Dynamics*, Vol. 42, No. 1, 2019, pp. 47–64. <https://doi.org/10.2514/1.G003686>.
- [55] Patel, P. R., and Scheeres, D. J., “Reachable and Fuel-Optimal Trajectory Estimates for Electric Propulsion Spacecraft,” *2023 IEEE Aerospace Conference*, 2023, pp. 1–11.

- [56] Patel, P. R., and Scheeres, D. J., “Rapid and Automatic Reachability Estimation of Electric Propulsion Spacecraft,” *The Journal of the Astronautical Sciences*, Vol. 70, No. 6, 2023, p. 45. <https://doi.org/10.1007/s40295-023-00408-5>.
- [57] Thangavelu, C., “Transfers between Near Rectilinear Halo Orbits and Low Lunar Orbits,” Master’s thesis, University of Colorado, Boulder, CO, 2019.
- [58] Wiesel, W. E., *Spaceflight dynamics*, 2<sup>nd</sup> ed., McGraw-Hill series in aeronautical and aerospace engineering, McGraw-Hill, New York, 1997.
- [59] Junkins, J. L., and Schaub, H., *Analytical Mechanics of Space Systems, Second Edition: Second Edition*, American Institute of Aeronautics and Astronautics, Reston, VA, 2009. <https://doi.org/10.2514/4.867231>.
- [60] Taheri, E., Kolmanovsky, I., and Atkins, E., “Enhanced Smoothing Technique for Indirect Optimization of Minimum-Fuel Low-Thrust Trajectories,” *Journal of Guidance, Control, and Dynamics*, Vol. 39, No. 11, 2016, pp. 2500–2511. <https://doi.org/10.2514/1.G000379>.
- [61] Andersson, J. A., Gillis, J., Horn, G., Rawlings, J. B., and Diehl, M., “CasADi: a software framework for nonlinear optimization and optimal control,” *Mathematical Programming Computation*, Vol. 11, 2019, pp. 1–36.
- [62] Jones, R., Curtis, D., and Zagaris, C., “Reachable Set Approximation in Cislunar Space with Pseudospectral Method and Homotopy,” *2023 IEEE Aerospace Conference*, IEEE, Big Sky, MT, USA, 2023, pp. 1–7. <https://doi.org/10.1109/AERO55745.2023.10115819>.
- [63] Trofimov, S., Shirobokov, M., Tselousova, A., and Ovchinnikov, M., “Transfers from near-rectilinear halo orbits to low-perilune orbits and the Moon’s surface,” *Acta Astronautica*, Vol. 167, 2020, pp. 260–271. <https://doi.org/10.1016/j.actaastro.2019.10.049>.
- [64] Mingotti, G., Sánchez, J., and McInnes, C., “Combined low-thrust propulsion and invariant manifold trajectories to capture NEOs in the Sun–Earth circular restricted three-body problem,” *Celestial Mechanics and Dynamical Astronomy*, Vol. 120, 2014, pp. 309–336. <https://doi.org/10.1007/s10569-014-9589-9>.
- [65] May, R. M., “Simple mathematical models with very complicated dynamics,” *Nature*, Vol. 261, No. 5560, 1976, pp. 459–467. <https://doi.org/10.1038/261459a0>.
- [66] Oblow, E., “Supertracks, supertrack functions and chaos in the quadratic map,” *Physics Letters A*, Vol. 128, No. 8, 1988, pp. 406–412. [https://doi.org/10.1016/0375-9601\(88\)90119-3](https://doi.org/10.1016/0375-9601(88)90119-3).
- [67] Koon, W., Lo, M., Marsden, J., and Ross, S., *Dynamical systems, the three-body problem and space mission design*, Interdisciplinary Applied Mathematics, Springer, 2011.
- [68] Singh, S., Junkins, J., Anderson, B., and Taheri, E., “Eclipse-Conscious Transfer to Lunar Gateway Using Ephemeris-Driven Terminal Coast Arcs,” *Journal of Guidance, Control, and Dynamics*, Vol. 44, No. 11, 2021, pp. 1972–1988. <https://doi.org/10.2514/1.G005920>.